



University of
Zurich^{UZH}

Discovery of a Collective Orbital Excitation in $\text{Ca}_3\text{Ru}_2\text{O}_7$

A Resonant X-ray Spectroscopy Study

MASTER THESIS

Department of Physics
University of Zurich

by

Karin von Arx

kvonar@physik.uzh.ch

under supervision of
Prof. Dr. Johan Chang
Dr. Masafumi Horio

Zurich, July 2019

Abstract

Ruddlesden-Popper type ruthenates $(\text{Sr,Ca})_{n+1}\text{Ru}_n\text{O}_{3n+1}$ are a class of strongly correlated electron systems where interactions between different degrees of freedom lead to a wealth of exotic electronic phenomena. Complexity in nature typically emerges from competing energy scales. In the ruthenates, the moderately localized valence d orbitals impose multi-orbital physics that is enriched by comparable energy scales of crystal field environment, spin-orbit and Hund's coupling. In the past decades, resonant inelastic x-ray scattering (RIXS) has developed rapidly as a technique to probe the relevant energy scales and the multi-orbital structure of various compounds.

This thesis presents a combined oxygen K -edge x-ray absorption spectroscopy and resonant inelastic x-ray scattering study of $\text{Ca}_3\text{Ru}_2\text{O}_7$. The low-lying electronic properties of Ru d orbitals were investigated by accessing them indirectly through their hybridization with O p orbitals. In this way, a new type of collective orbital excitation has been discovered in $\text{Ca}_3\text{Ru}_2\text{O}_7$. By comparison to similar experiments on Ca_2RuO_4 , it is shown that the excitation spectrum of $\text{Ca}_3\text{Ru}_2\text{O}_7$ is unique for that compound. This finding is likely linked to the different electronic and magnetic ground states of $\text{Ca}_3\text{Ru}_2\text{O}_7$ and Ca_2RuO_4 . The work presented here elucidates the important orbital degrees of freedom and offers a direct comparison of structurally closely related ruthenates.

Zusammenfassung

Ruthenate $(\text{Sr,Ca})_{n+1}\text{Ru}_n\text{O}_{3n+1}$ der Ruddlesden-Popper Phase sind eine Klasse von stark korrelierten Elektronensystemen, bei denen die Interaktion zwischen den verschiedenen Freiheitsgraden zu einer Vielzahl von exotischen elektronischen Phänomenen führt. In der Natur entsteht Komplexität üblicherweise aus gegeneinander konkurrierenden Energieskalen. In den Ruthenaten werden multi-orbital Effekte durch die mässig lokalisierten d Valenzorbitale auferlegt und hinzu kommen auch die vergleichbaren Energieskalen der Kristallfeld Umgebung, Spin-Bahn und Hund's Wechselwirkungen. In den letzten Jahrzehnten hat sich resonante inelastische Röntgenstreuung (RIXS) als Messmethode rasant entwickelt, um die relevanten Energieskalen und multi-orbital Strukturen von verschiedenen Verbindungen zu untersuchen.

In dieser Arbeit wird eine Kombination von Sauerstoff K -Kanten Röntgenabsorptionsspektroskopie- und resonanter inelastischer Röntgenstreuungsstudien von $\text{Ca}_3\text{Ru}_2\text{O}_7$ präsentiert. Die niedrig gelegenen elektronischen Eigenschaften von Ru d Orbitalen werden untersucht, indem sie indirekt über ihre Hybridisierung mit O p Orbitalen erreicht werden. Auf diese Weise konnte eine neue Art von kollektiven orbitalen Anregungen in $\text{Ca}_3\text{Ru}_2\text{O}_7$ entdeckt werden. Durch den direkten Vergleich zu ähnlichen Experimenten an Ca_2RuO_4 konnte gezeigt werden, dass das Anregungsspektrum von $\text{Ca}_3\text{Ru}_2\text{O}_7$ spezifisch für diese Verbindung ist. Dieses Ergebnis steht möglicherweise in Zusammenhang mit den unterschiedlichen elektronischen und magnetischen Grundzuständen von $\text{Ca}_3\text{Ru}_2\text{O}_7$ und Ca_2RuO_4 . Die hier vorgestellte Arbeit erläutert die wichtigen orbitalen Freiheitsgrade und ermöglicht einen direkten Vergleich von eng verwandten Ruthenaten.

Contents

| | |
|---|-----------|
| Abstract | 3 |
| Zusammenfassung | 5 |
| Contents | 6 |
| 1. Introduction | 9 |
| 1.1. Strongly Correlated Electron Systems | 9 |
| 1.2. Ruthenates | 11 |
| 1.2.1. Mott Mechanism of Ca_2RuO_4 | 12 |
| 1.2.2. Elusive Semimetallic State of $\text{Ca}_3\text{Ru}_2\text{O}_7$ | 13 |
| 1.3. Thesis Outline | 15 |
| 2. Experimental Methods | 17 |
| 2.1. X-ray Absorption Spectroscopy | 17 |
| 2.2. Resonant Inelastic X-ray Scattering | 19 |
| 2.2.1. Physical Process | 20 |
| 2.2.2. Instrumentation | 21 |
| 2.2.3. Data Evaluation | 23 |
| 2.2.4. Second Order Perturbation Scattering Theory | 26 |
| 2.3. Sample Preparation | 29 |
| 3. Results | 31 |
| 3.1. XAS Measurements | 31 |
| 3.1.1. Absorption Edge and Orbital Selectivity | 31 |
| 3.1.2. Absorption Spectra of $\text{Ca}_3\text{Ru}_2\text{O}_7$ | 34 |
| 3.1.3. Comparison to Ca_2RuO_4 | 36 |
| 3.1.4. Discussion | 38 |
| 3.2. RIXS Measurements | 39 |
| 3.2.1. Excitations in Different Experimental Conditions | 39 |
| 3.2.2. Momentum Dispersion of Lowest Energy Excitation | 42 |
| 3.2.3. Comparison to Ca_2RuO_4 | 43 |
| 3.2.4. Discussion | 45 |
| 4. Conclusion and Outlook | 47 |

| | |
|---|-----------|
| Appendix | 49 |
| A. Absorption Resonance Energy | 49 |
| B. Analysis of B Excitation | 50 |
| C. Charge-Density-Wave Order in LESCO | 51 |
| D. Free-Electron Laser Experiments | 53 |
| References | 54 |
| Acknowledgements | 61 |

1. Introduction

Technological advancement and progress have always been closely linked to the materials exploited by human mankind. Since the stone age when humans first used tools craved out of stone over the Bronze and Iron age up to the present Silicon Age, the understanding and usage of materials was the cornerstone for human development. For instance, the technological progress that lead to digitalization forming our current society was based on the fundamental understanding of semiconductors like silicone. Nowadays, a main pillar of modern science is condensed matter physics, devoted to the study and understanding of the microscopic mechanisms in solids and liquids. This lays the ground for controlled manipulation of their properties for new technological applications.

1.1. Strongly Correlated Electron Systems

One of the most challenging but deeply intriguing field of condensed matter physics addresses strongly correlated electron systems. Whereas in conventional metals or semi-metals the electrons can be treated approximately as free particles in the periodic potential of the atomic nuclei, in strongly correlated systems the interactions between different degrees of freedom impose more complexity and a complete solution of the many-body problem is not feasible anymore. However, it is the incorporation of the strong interactions that leads to a vast variety of fascinating phenomena and makes these materials such a rich and widely studied area of condensed matter physics. Probably the most famous example are superconductors (SC): their electric resistivity drops to zero below a certain transition temperature due to a delicate net attraction of conduction electrons which is mediated by crystal lattice vibrations in the case of conventional SC. In addition to the resistivity drop, SC also actively exclude magnetic field lines from their interior when cooled below the transition temperature. This phenomenon is called the Meissner effect. Since their discovery at the beginning of the last century by H. K. Onnes [1] a lot of attention and effort have been put into their research and up to the present, superconductivity has been found in many different compounds. The dream of superconductivity at room temperature has come within reach after the sensational discovery of high temperature superconductors

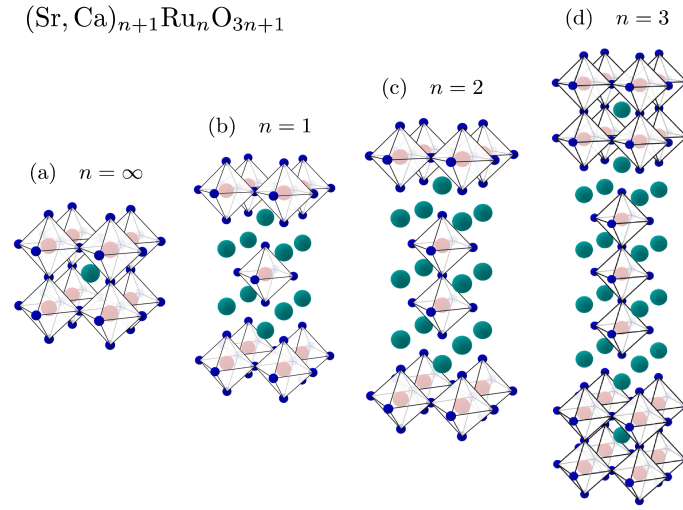


Figure 1.1.: Illustration of the Ruddlesden-Popper crystal structure of $(\text{Sr}, \text{Ca})_{n+1}\text{Ru}_n\text{O}_{3n+1}$ for $n = \{\infty, 1, 2, 3\}$. Green, red and blue atoms are Sr or Ca, Ru and O atoms, respectively. Taken from Ref. [8].

and their improvement in transition temperature ever since. Regarding the theory behind superconductivity, the famous BCS theory is successful to describe normal superconductivity arising from a lattice vibration mediated pairing mechanism on a microscopic level. However, new types of superconductors have been found that seem to have a different pairing mechanism and symmetry. Up to now, this unconventional superconductivity has not been fully understood and drives one of the main research fields in condensed matter. However, superconductivity is not by far the only interesting phenomena that can be observed in strongly correlated materials. They often have an extremely rich phase diagram with exotic electronic and magnetic properties such as Mott insulating phases, spin and orbital orders, colossal magnetoresistance and quantum criticality [2, 3, 4].

At the root of big variety in physics usually lie the localized valence shells of the metal atoms in these compounds. While s and p orbitals typically interact strongly with neighbouring atoms resulting in large bandwidths, f shells are tightly bound to the nucleus. In between the d orbitals have itinerant and localized properties [5]. Here, the charge, spin and orbital degrees of freedom can still be described in a localized picture, but they are able to interact with neighbouring ions. This complex interplay is the reason for the intricate wealth of phenomena exhibited by correlated materials with valence d shells. In particular, the correlation effects in $4d$ transition metal oxides (TMO), to which class the ruthenates studied in this thesis belong, are weak compared to $3d$ TMOs but in the same order of magnitude as the bandwidth or crystal field splitting. Consequently, there is a constant competition of these energy scales and even small perturbations such as magnetic field, doping or pressure

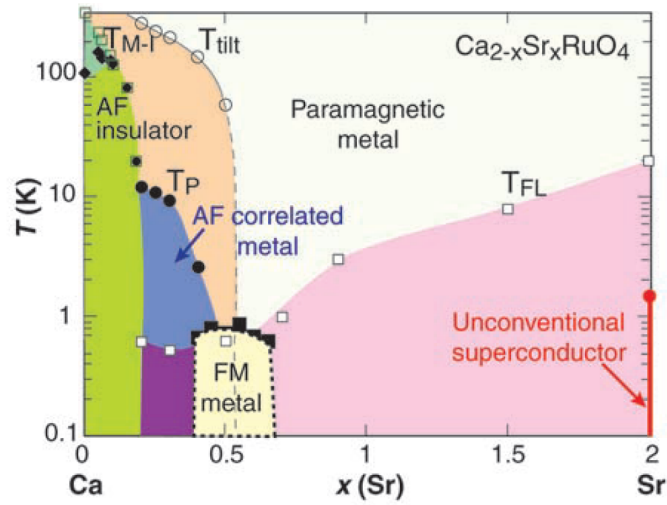


Figure 1.2.: Phase diagram of $\text{Ca}_{2-x}\text{Sr}_x\text{RuO}_4$. It covers the whole range from insulating ($x = 0$) over correlated and Fermi liquid (FL) metallic behaviour up to superconductivity ($x = 2$). The magnetic structures cover all antiferromagnetic (AF), ferromagnetic (FM) and paramagnetic ordering. Taken from Ref. [9].

have a huge impact on the characteristics of such compounds [6]. This behaviour explains the rich phase diagrams of these materials which make them one of the most interesting but at the same time one of the most complex systems to study. Also from the theoretical point of view they are extremely challenging, since density functional theory fails to describe their physics and new approaches like dynamical mean-field theory had to be developed [7].

1.2. Ruthenates

A prominent and widely studied class of TMO's are the ruthenates. Particularly interesting are the Ruddlesden-Popper series of the form $(\text{Sr,Ca})_{n+1}\text{Ru}_n\text{O}_{3n+1}$ where n layers of the perovskite lattice $(\text{Sr,Ca})\text{RuO}_3$ are interleaved by a spacer layer, as depicted in Fig. 1.1. As mentioned above, these systems have extremely rich phase diagrams with exotic ground states as shown in Fig. 1.2 for the single layer compound series $\text{Ca}_{2-x}\text{Sr}_x\text{RuO}_4$. The phases range from unconventional superconductivity on the Sr side ($x = 2$) to the antiferromagnetic Mott-insulator on the Ca side ($x = 0$).

Generally, in the materials of the Ruddlesden-Popper series, the octahedral crystal field environment of the transition metal lifts the degeneracy of the Ru d orbitals. At lower energy are the t_{2g} states composed of d_{xy} , d_{xz} and d_{yz} orbitals whereas the e_g orbitals d_{z^2} and $d_{x^2-y^2}$ lie at higher energy [10], see Fig. 1.3. Here, four electrons occupy the Ru valence states in the t_{2g} orbitals leading to a $2/3$ occupancy.

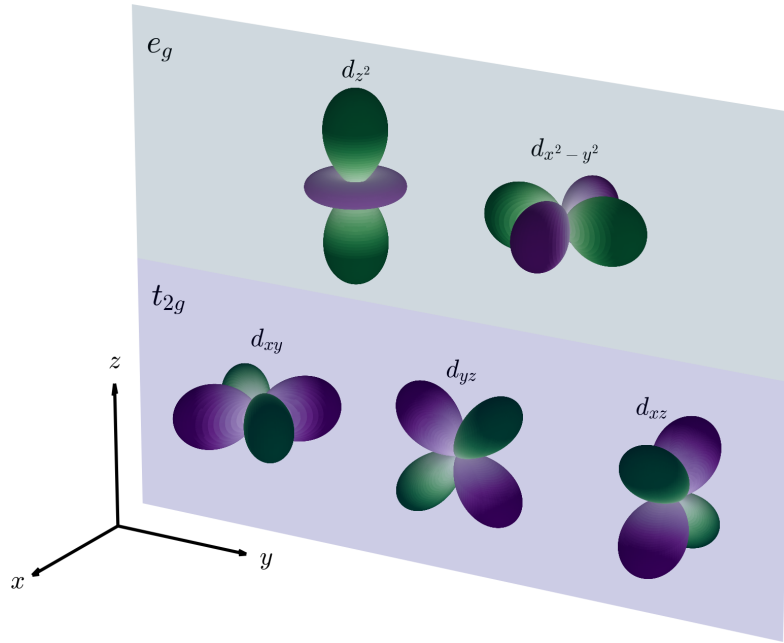


Figure 1.3.: d orbitals in an octahedral crystal field environment. The fivefold degeneracy is lifted and the two e_g states are left at a higher energy than the three t_{2g} states. Taken from Ref. [8].

To understand the exotic phenomena arising in ruthenates, it is vital to have knowledge of the electronic structure, structural distortions and orbital and spin-orbital interactions. The focus usually is on the ruthenium bands as they are responsible for strong correlations and magnetic moment formation.

In this thesis, the single layer Ca_2RuO_4 and the bilayer $\text{Ca}_3\text{Ru}_2\text{O}_7$ are investigated by resonant inelastic x-ray scattering to shed light on the energy scales of different interactions within the Ru d bands. Below, the two compounds are introduced to give an overview of their ground states and emerging phenomena.

1.2.1. Mott Mechanism of Ca_2RuO_4

In single layer Ca_2RuO_4 , the crystal shows lattice distortions in form of rotation and tilt of the RuO_6 octahedra compared to the undistorted crystal structure of Sr_2RuO_4 and has lattice constants $a = 5.39 \text{ \AA}$, $b = 5.63 \text{ \AA}$ and $c = 11.75 \text{ \AA}$ [11]. The tilt of the octahedra is primarily in the ac -plane and only slightly in the bc -plane. Both distortions are due to the smaller ionic radius of Ca compared to Sr. They reduce the hopping matrix element and hence enhance correlation effects. This in return has a huge impact on the ground state of this compound. When Ca_2RuO_4 is cooled down, it undergoes a first-order structural transition at $T_s = 356 \text{ K}$, compressing the

c -axis lattice parameter by around 1.2% [12]. The compression lowers the energy of the d_{xy} orbital relative to that of the d_{yz} and d_{xz} orbitals. This triggers an almost fully occupied d_{xy} orbital which opens for a Mott insulating transition in the half filled d_{xz} and d_{yz} bands. Between $T = 356$ K and 110 K Ca_2RuO_4 is a paramagnetic insulator before it enters a G-type AFM ordered phase at $T_N = 110$ K [11]. In this type of antiferromagnetism, the magnetic moments are antiferromagnetically aligned in-plane as well as in the out-of-plane direction. To understand the Mott insulating state and the mechanism behind the gap opening within the d bands from a theoretical point of view, it is important to take into account many different interactions. Not only the relative value of Coulomb repulsion U and bandwidth W , but also the crystal field Δ , spin-orbit-coupling λ and Hund's coupling J_H have to be considered. The Hund's coupling describes the intra-atomic exchange interaction and has been shown to play an important role in different correlated materials [13]. Hence, this system goes beyond the standard Mott theory and is of great interest to explore the complex interplay of comparable and thus competing energy scales.

1.2.2. Elusive Semimetallic State of $\text{Ca}_3\text{Ru}_2\text{O}_7$

In the Ruddlesden-Popper series the bilayer $\text{Ca}_3\text{Ru}_2\text{O}_7$ stands in between the metallic paramagnetic CaRuO_3 [15] and the Mott insulating antiferromagnetic Ca_2RuO_4 introduced above. As in Ca_2RuO_4 , the RuO_6 octahedra are rotated and tilted due to the small Ca radius, see Fig. 1.4 (a). The lattice parameters are $a = 5.37$ Å, $b = 5.54$ Å and $c = 19.52$ Å [16]. In contrast to the single layer, $\text{Ca}_3\text{Ru}_2\text{O}_7$ undergoes first a magnetic transition upon cooling at $T_N = 56$ K entering an antiferromagnetic state. However, the in-plane magnetic moments are not aligned antiferromagnetically as in Ca_2RuO_4 but ferromagnetically within the double layer while antiferromagnetically between the double layers [16, 17]. This structure is the so-called A-type AFM. This difference in the in-plane magnetic order implies that the interaction within the double layer plays an important role for the magnetic ground state and further investigation of the energy scales defining the microscopic interactions is of great interest.

Upon further cooling, a first order structural transition takes place at $T_s = 48$ K. This transition was often referred to as a metal-insulator transition [18, 19, 20] although the system is not going fully insulating but remains poorly metallic down to lowest temperatures. More specifically, the behaviour of the resistivity is highly anisotropic as can be seen in Fig. 1.4 (b). The motivation for referencing it as metal-insulator transition may lie in the steep up-rise of the out-of-plane resistivity ρ_c at the transition temperature. This behaviour of ρ_c is surprising considering that the c -axis is compressed which should lead to larger orbital overlap in the out-of-plane

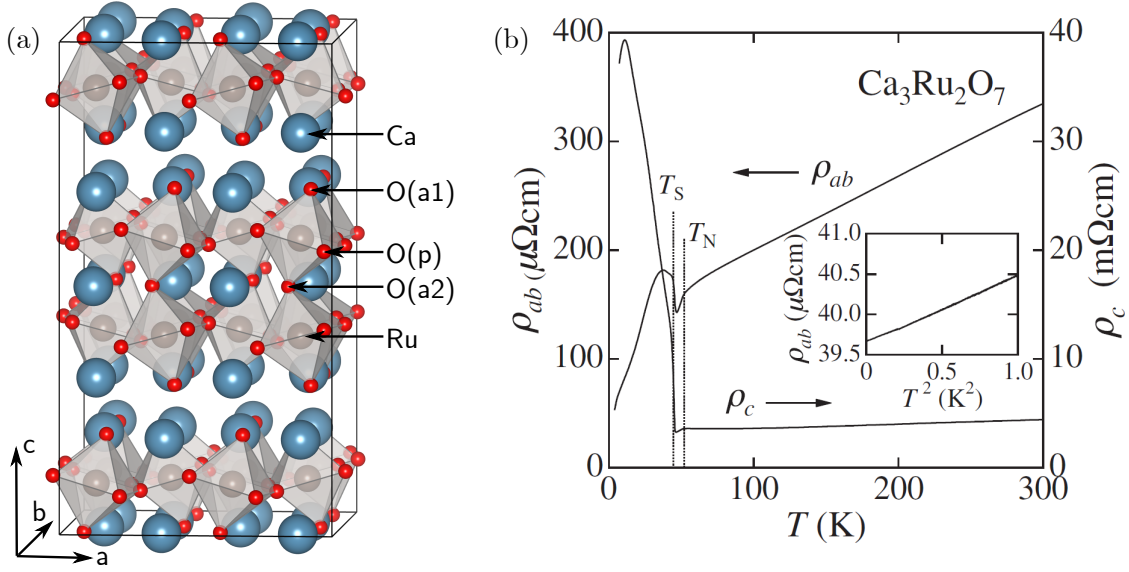


Figure 1.4.: (a) Crystal structure of $\text{Ca}_3\text{Ru}_2\text{O}_7$. There are three different oxygen sites: one planar (O(p)), and two apical (inner O(a2) and outer O(a1)). (b) Temperature dependence of in-plane and out-of-plane resistivity in $\text{Ca}_3\text{Ru}_2\text{O}_7$. Taken from Ref. [14]

direction and hence enhance electron itinerancy. In contrast, the in-plane resistivity ρ_{ab} is only increasing slightly first and then dropping below 30 K. Recently, it has been shown that there is even an anisotropy in the in-plane resistivity between ρ_a and ρ_b [21]. This puzzling anisotropic behaviour and the additional transition at 30 K have not been fully understood yet and an explanation on a microscopic level is still lacking. At low temperature, the quasi-two-dimensional metallicity seems to emerge from small Fermi surface pockets as it was observed in quantum oscillation experiments [22, 23]. In disagreement to this, ARPES measurements report boomerang-like Fermi arcs [24]. Even though $\text{Ca}_3\text{Ru}_2\text{O}_7$ does not undergo a full Mott transition like Ca_2RuO_4 , the lattice response across T_s is very similar with a c -axis lattice parameter compression. The effect is however one order of magnitude smaller in $\text{Ca}_3\text{Ru}_2\text{O}_7$ with around 0.1% compared to 1.2% in Ca_2RuO_4 [16]. Also worth mentioning is the fact that upon the transition, both in-plane and out-of-plane Ru-O bond lengths jump in Ca_2RuO_4 , whereas there is no significant change observed in the case of $\text{Ca}_3\text{Ru}_2\text{O}_7$. These structural differences may be part of the reason for the different physical behaviour of these two compounds.

Another interesting phenomenon arising in this compound is the colossal magnetoresistance [23, 25, 26]. But it has to be mentioned that the behaviour of $\text{Ca}_3\text{Ru}_2\text{O}_7$ upon application of magnetic field is highly anisotropic. Changing the direction of the magnetic field along the different crystallographic axes drives the system either in a canted antiferromagnetic metallic phase ($B \parallel b$), exhibits the already mentioned

colossal magnetoresistance ($B||a$) or Shubnikov-de Haas oscillations ($B||c$) [26, 27]. When $\text{Ca}_3\text{Ru}_2\text{O}_7$ is doped with Ti, the Mott insulating state can be achieved and the magnetic structure transforms from A-type to G-type AFM. Applying a modest magnetic field to this compound leads to a collapse of the Mott insulating state and a negative colossal magnetoresistance is observed [19].

1.3. Thesis Outline

To develop new technologies and applications, the discovery of new phenomena alone is not sufficient. It requires the fundamental understanding of the material's properties to the extent that they can be manipulated to the respective needs. In this context, the research on calcium ruthenates is dedicated to the understanding of the microscopic processes behind the exotic phenomena arising in their phase diagrams. One major part of the mechanism behind different transport and magnetic properties exploited in technology are the electronic structures. Especially important for potential applications is the excitation spectrum of the electrons that displays the effects and processes that take place when the system is energetically excited. Measurements like resonant inelastic x-ray scattering address this by identifying the low energy spin and orbital excitations.

This thesis focuses on oxygen K -edge x-ray absorption spectroscopy (XAS) and resonant inelastic x-ray scattering (RIXS) measurements of Ca_2RuO_4 and $\text{Ca}_3\text{Ru}_2\text{O}_7$. It presents new data on the bilayer $\text{Ca}_3\text{Ru}_2\text{O}_7$ that were analysed and interpreted within the work of this thesis, and compares this data to recent studies on the single layer Ca_2RuO_4 . Both datasets were measured at the ADRESS beamline of the Swiss Light Source synchrotron in Switzerland.

The thesis starts with a description of the experimental methods employed to measure the data presented here, namely XAS and RIXS. The second part about RIXS includes introduction of the underlying physical process, the instrumentation and data analysis tools needed for the experiments as well as the theory behind the scattering process.

Chapter 3 presents experimental results of $\text{Ca}_3\text{Ru}_2\text{O}_7$, their discussion and the comparison to Ca_2RuO_4 . The first section is devoted to the XAS results, starting with a detailed discussion about the choice of the absorption edge and orbital selectivity through hybridization of O p with Ru d orbitals. Then the absorption spectra of $\text{Ca}_3\text{Ru}_2\text{O}_7$ are analysed for different experimental geometries and light polarizations to determine the energy scales of the Ru d orbitals. The differences to Ca_2RuO_4 spectra are analysed and discussed. The absorption resonances identified in the XAS spectra are used to set the photon energy for the RIXS measurements

presented in the second section. The RIXS data of $\text{Ca}_3\text{Ru}_2\text{O}_7$ comprise spectra taken under different geometries, polarizations and temperatures to measure the evolution of the excitations. The analysis of the low energy features reveals a momentum dependence of the lowest excitation. The findings of $\text{Ca}_3\text{Ru}_2\text{O}_7$ are then again compared to recent studies of Ca_2RuO_4 .

Lastly, in chapter 4 the conclusions are summarized and an outlook for future experiments is given.

2. Experimental Methods

This chapter introduces the two experimental methods employed in this study: x-ray absorption spectroscopy (XAS) and resonant inelastic x-ray scattering (RIXS). The combination of these methods allows to probe site-specific elementary excitations in complex materials energy and momentum resolved. After a brief introduction to XAS, the focus is on a detailed description of the RIXS technique, including the physical process, the instrumentation at the ADDRESS beamline of the Swiss Light Source and the theory of RIXS.

2.1. X-ray Absorption Spectroscopy

Every RIXS experiment starts with a XAS measurement to determine the absorption edge. While varying the incident photon energy E , the absorption spectrum is measured. Every time the photon energy E equals the binding energy of a core electron in the material, the interaction cross section is enhanced and the absorption shows a sharp increase. This so-called absorption edge is due to annihilation of the photon by creating a photoelectron and a core-hole. The XAS technique thus probes unoccupied electronic states of the material under investigation. Above the absorption edge, the difference between the photon energy and the binding energy goes into kinetic energy of the photoelectron and the absorption decreases again. On a femtosecond timescale, the excited states decay and the core-hole is filled by an electron from a higher energy level. The excess energy is released by fluorescence x-ray or Auger electron emission.

Generally, the edges occur at the binding energy of all core levels. They are classified by the principal quantum number n of the core electron which is excited: $n = 1, 2$, and 3 correspond to the K -, L -, and M -edges, respectively. The energy of each edge is in strong correspondence to the atomic levels of the element and increases roughly with Z^2 , Z being the atomic number, see Fig. 2.1 (a). This means that the technique is element-specific and by choosing the photon energy one chooses the element inside the material that is investigated. Furthermore, the exact binding energy is site dependent. This is due to the different crystal field environment the

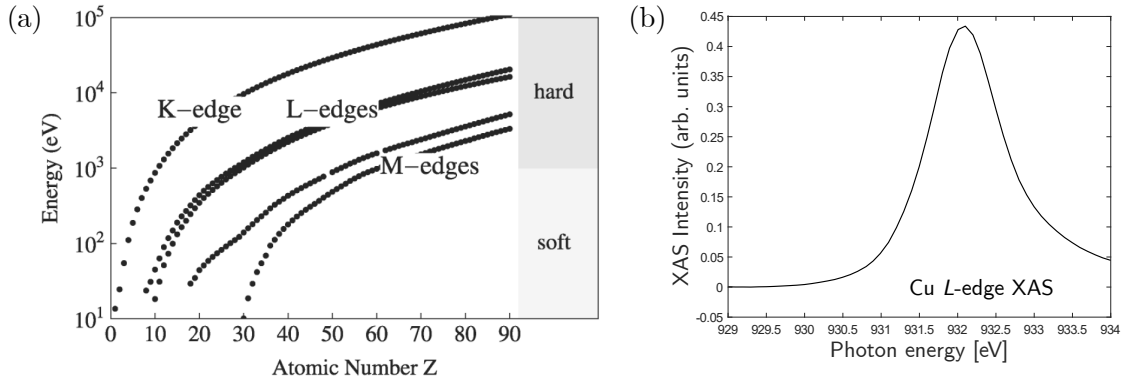


Figure 2.1.: (a) Energy of different x-ray absorption edges as a function of atomic number Z . Taken from Ref. [28]. (b) Copper L -edge absorption spectrum of $\text{La}_{2-x}\text{Sr}_x\text{CuO}_4$ with a doping of $x = 14.5\%$. Recorded at the ADRESS beamline of the Swiss Light Source, 2019.

elements experience at different crystallographic sites. For example, the oxygen in a layered perovskite structure (Fig. 1.4 (a)) can occupy a planar or apical site which results in distinguishable features in the absorption edge spectrum. Fig. 2.1 (b) shows a copper L -edge absorption spectrum of $\text{La}_{2-x}\text{Sr}_x\text{CuO}_4$ as a general example for a XAS spectrum. Below 931 eV, the energy of the photon is not high enough to excite an electron in the copper $2p$ level to an unoccupied state. From 931 eV and higher energies, the electrons get excited and the detected intensity is non zero.

Beside the energy characteristics of this method, the orbital character of the core electron also plays an important role. Because the initial core state of the electron has a well defined symmetry, the selection rules of the transition define the symmetry of the final state in the continuum. According to the dipole selection rule, the final state's orbital momentum l must increase or decrease by a quantum $\Delta l = \pm 1$. For instance, excitation of a $1s$ electron at the K -edge promotes it into an initially unoccupied final orbital state with strong p character. This selectivity gives the opportunity not only to study the energy levels of the unoccupied states, but also orbital character and hybridizations.

Experimentally, an XAS spectrum can be obtained in different ways. The most direct way of measuring the absorption in transmission mode is usually unpractical because homogeneously thin samples are required. Additionally, the RIXS experiment afterwards is mostly done in reflection mode. Therefore, the more convenient methods are based on reflection measurements and make use of the relaxation process that follows the absorption. The core hole that is left after the absorption is filled on a femtosecond timescale by an electron in the valence band of the system. This electron thus decays from a valence state into a core state with much higher binding

energy and the energy difference is released in two ways: either a photon is emitted (fluorescence) or the energy is transferred to another electron which is then promoted in an unoccupied state and eventually escapes into vacuum (Auger electrons). The indirect XAS measures these decay products, the emitted photon or the electron and can therefore be operated in fluorescence yield mode or electron yield mode.

In total electron yield mode, the emitted electrons, which can be photoelectrons, secondary electrons or Auger electrons, are measured. Because the samples are routinely grounded, the emitted electrons are replaced and one can measure the current flowing from the ground to the sample. The amount of electrons detected with this method is proportional to the number of absorbed photons. In this way, the Fermi level of the system is not affected by the process and charge neutrality is preserved.

In total fluorescence yield mode, the intensity of the emitted x-rays from the radiative relaxation of the core hole is measured by a photodiode. The intensity of this fluorescence line is proportional to the absorption, but a finite solid angle and a broad range of photon energies are integrated. This means that the fluorescence yield intensity corresponds to the integrated RIXS intensity at the same incident energy. One complication in fluorescence mode is the self-absorption that has to be taken into account for both XAS and RIXS measurements. The emitted photon can be re-absorbed by the sample and this reduces the measured intensity. Self-absorption depends strongly on experimental geometry because the travelling distance of the photon inside the sample depends on incoming and outgoing angle.

2.2. Resonant Inelastic X-ray Scattering

Resonant inelastic x-ray scattering (RIXS) is a fast developing *photon-in photon-out* synchrotron based spectroscopy in which one scatters x-ray photons inelastically off matter and detects the scattered photon. By measuring the changes in photon energy, momentum and polarization which are transferred to the material under study, this technique provides substantial information about the intrinsic excitation spectrum. The main principle lies in tuning the incident photon energy such that it coincides with one of the atomic x-ray transitions of the system, so-called absorption edges. Not only does this enhance the scattering cross-section but it also makes the process element-specific allowing to probe charge, magnetic and orbital degrees of freedom on selected atomic species.

RIXS has a number of unique features that make it advantageous and extremely powerful compared to other scattering techniques. Firstly, as mentioned above it is

element and orbital sensitive by setting the incident photon energy to an element-specific absorption edge. RIXS can even be sensitive to inequivalent bondings or inequivalent crystallographic positions of the same chemical element if the absorption edges are distinguishable. Other advantages are the bulk sensitivity and the small sample volumes that can be measured [28].

The main limitation of RIXS is the energy resolution, which is determined by both the availability of tunable photon sources that provide a high enough photon flux and the availability of the instrumentation to energy resolve the scattered photons. In addition, the reciprocal space that can be measured is usually limited to the first Brillouin zone due to the scattering geometry. However, the RIXS resolution has improved considerably over the years and currently a resolution of ~ 35 meV at Cu L_3 edge can be achieved at the European Synchrotron Radiation Facility (ESRF) [29].

2.2.1. Physical Process

In the microscopic picture of the RIXS process, the incoming photon is tuned to resonate with an absorption edge of the material under study and promotes a core electron into an empty valence shell. The system is now in an excited intermediate state with a hole deep in the electronic core and will therefore decay quickly from this intermediate state. The decay can occur in a number of different ways. In the channel relevant for RIXS, the empty core state is filled by an electron and a photon is emitted. The energy of the emitted photon $\hbar\omega_{out}$ depends on the relaxation process. If the same electron that was promoted to the valence shell by the absorption process decays back into the core level, the energy of the outgoing photon will be the same as the incident one. This process is called an elastic scattering event. However, if an electron from a different, initially occupied valence state annihilates the core hole, the emitted photon has a lower energy than the incident one and the process is inelastic, see Fig. 2.2. As a result, the system is left with an electron-hole excitation. This excitation can propagate through the material with an energy $\hbar\omega = \hbar(\omega_{in} - \omega_{out})$ and momentum $\hbar q = \hbar(k_{in} - k_{out})$ [28]. By detecting the outgoing photon in specific angles to the incoming photons, the transferred momentum $\hbar q$ can be selected and excitations can be measured in a momentum dependent fashion.

A summary of the different elementary excitations that can be accessed with the inelastic process described above is shown in Fig. 2.3. A very broad class of excitations can be studied including plasmons, charge transfer excitations, crystal-field and orbital excitations, magnons and phonons. All these excitations are overall charge neutral since the scattered photons do not add or remove charge.

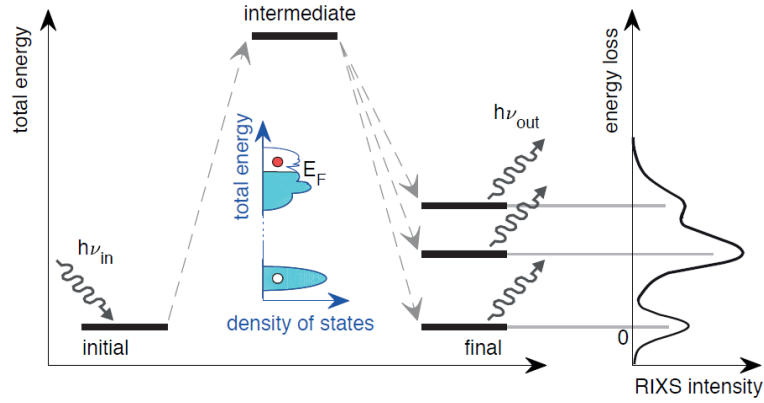


Figure 2.2.: Schematic depiction of the RIXS process. The excited intermediate state can decay in a final state with less energy than the initial state if an electron from the initially occupied valence band decays into the core hole. Taken from Ref. [30].

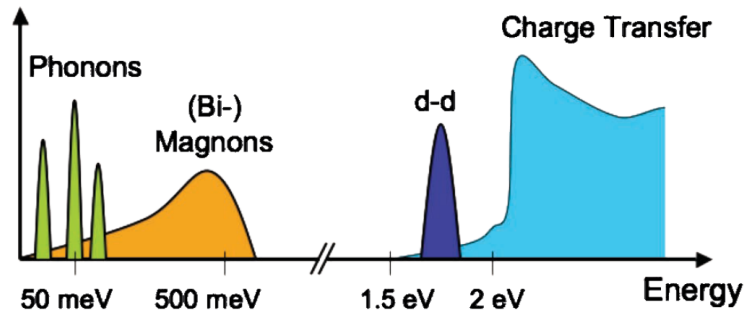


Figure 2.3.: Elementary excitations that are accessible by RIXS and their approximate energy scales. Taken from Ref. [28].

2.2.2. Instrumentation

In a RIXS experiment, a monochromatic photon beam is focused on the sample and the scattered beam is then detected energy resolved in a specific scattering angle. The RIXS instrument is therefore divided in two parts: the beamline which provides a well-collimated, focused and highly monochromatic beam and the spectrometer which includes the sample environment, focusing, energy dispersion of the scattered beam and the detector. Depending on the absorption edges and therefore the photon energy that is used, it can be differentiated further between hard and soft RIXS instruments. Hard x-ray instruments use Bragg crystal optics where the highly ordered crystalline lattice of Si or Ge is used to achieve very high energy resolution. Such schemes do not work in the soft x-ray regime, since the longer wavelength prohibits the use of crystal optics. Instead, diffraction gratings are utilized.



Figure 2.4.: (a) Schematics of a RIXS spectrometer using a spherical grating. Taken from Ref. [32]. (b) Sketch of the spatial resolution improvement by tilting the detector. Adapted from Ref. [33].

In this section, the soft x-ray RIXS endstation at the ADDRESS beamline of the Swiss Light Source, where the experiments presented in this thesis were performed, is discussed in detail.

The ADDRESS beamline delivers soft x-ray radiation with a photon energy ranging from approximately 400 to 1600 eV. The photon source is a fixed-gap undulator with four permanent magnetic arrays that can be shifted in the longitudinal direction, allowing to set the energy without changing the gap and having full control over the polarization. The beamline optics adopt the scheme of plane-grating monochromator operating in collimated light and ensure a highly monochromatic beam with high flux and small spot size [31].

After scattering off the sample, the photons are analysed by the high-resolution spectrometer called SAXES [34]. It is based on a variable line spacing (VLS) spherical grating to energy disperse the beam and provide focusing onto the two dimensional detector. Photons with different energies are thereby scattered off the grating in different directions such that the vertical impact location on the detector corresponds to the energy of the photon, see Fig. 2.4 (a). The ADDRESS beamline has two gratings with different line spacings in operation. The first one has an average groove density of 3200 lines/mm and is optimized for high-resolution measurements around the Cu L_3 -edge. The second grating has a lower groove density of 1500 lines/mm to enhance reflectivity and thus compensate for the lower cross-section of softer x-rays [35]. The detector RIXSCam from XCAM Ltd. is an electron-multiplying charge coupled device (CCD) that consists of three horizontally arranged chips with 1608×1632 pixels each. The advantage of using three chips next to each other is better statistics and therefore reduced acquisition time. The pixel size is $16 \mu\text{m} \times 16 \mu\text{m}$. To enhance the spacial resolution, and thus the energy resolution, the detectors are mounted at an angle of 20° with respect to the optical axis which reduces the effective pixel size, see Fig. 2.4 (b). Because of the diffusion of the charge cloud that is produced by a single photon in the field free region of the CCD, the signal is shared by multiple pixels. Therefore, a centroiding algorithm is used to determine a

sub-pixel position of interaction. This single-photon counting software then allows to divide each pixel in four sub-pixels [36]. Overall, the achieved effective sub-pixel size is less than $2\text{ }\mu\text{m}$ [32].

Beside the energy dispersing feature of the spectrometer, it also allows for varying the scattering angle of incoming and outgoing photons between 25° and 130° . For this, the 4 m long dispersion arm is mounted on a rotating girder platform and thus the dispersion of low-energy excitations can be measured as a function of momentum transfer.

2.2.3. Data Evaluation

Following, the procedures to analyse the data are shortly presented. First, it is explained how the energy scale of each spectra is correctly set and how the intensity is normalized, allowing to qualitatively compare different spectra. Second, the calculation of the momentum that is transferred to excitations inside the sample is demonstrated.

Energy Calibration

As explained above, the photons scattered off the sample are vertically energy dispersed by reflection on a grating and then detected by a CCD camera. Thus, the height of the detector determines the energy range which is measured and needs to be adjusted when the photon energy is changed. In the spectrum recorded by the detector, each channel corresponds to a specific photon energy and the difference between two neighbouring channels in the oxygen *K*-edge experiment presented in this thesis is equal to 45 meV. This energy per pixel varies for different photon energy settings of the whole spectrometer and therefore needs to be remeasured after every change of the absorption edge. The method to determine the energy per pixel is a measurement on carbon tape. There, the resolution limited, intense elastic peak on the detector is measured for different incoming photon energies. In addition to the energy per pixel, this method also allows for the determination of the energy resolution of the experiment as the full width at half maximum (FWHM) of the elastic peaks. The absolute energy of one pixel is not known *a priori*, depends on the detector height and can drift during a long measurement. Because of this, it is necessary to evaluate the energy corresponding to a specific pixel for each spectrum in the data analysis process. Fig. 2.5 illustrates how this is done. Since the probability for a photon to gain energy in the scattering process is negligibly small for our conditions, the value of the incoming photon energy is the upper limit for the detected energies and the first signal from the high energy side is the elastic

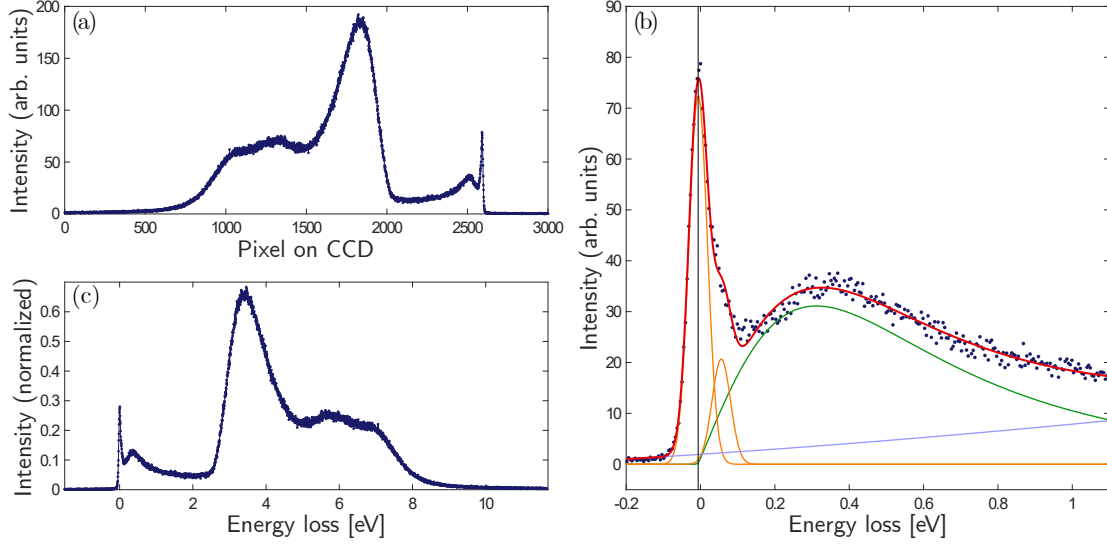


Figure 2.5.: Energy scale calibration. (a) Raw data as it is detected by the CCD camera. Intensity is recorded as a function of vertical pixel. (b) After converting pixel into energy and setting a rough zero energy loss position, the low energy part of the spectrum is fitted with two Gaussians (orange), a DHO (green) and a quadratic background (light blue) to find the exact zero energy loss position as the centre of the first Gaussian (indicated by vertical line). (c) Spectrum shifted to match the exact zero energy loss position. The intensity is normalized to the dd excitation.

peak $\hbar\omega_{in} = \hbar\omega_{out}$. Here, the high energy side corresponds to higher pixel number. The elastic peak can therefore be used to set the zero energy loss in the spectrum. In the case of calcium ruthenate spectra, the elastic peak overlaps with low energy excitations. Thus, the fitting needs to include contributions from these excitations in order to guarantee an exact determination of the centre of the elastic peak. For the RIXS data presented in this thesis, the zero energy was first set roughly to the first peak and then the low energy part is fitted with four contributions to determine the exact position of the elastic peak (Fig. 2.5 (b)). The contributions are two Gaussians for the elastic peak and the lowest excitation, a response function of a damped harmonic oscillator (DHO) [37] and a quadratic function to describe the background. The width of the first Gaussian is always fixed to the energy resolution determined by the carbon tape measurement. In order to find the right zero energy loss position, it is important that the left side of the first peak is described well by the first Gaussian as it represents only elastic scattering. After the energy scale is set, the intensity is normalized to the dd excitation peak between 2.2 – 5 eV energy loss.

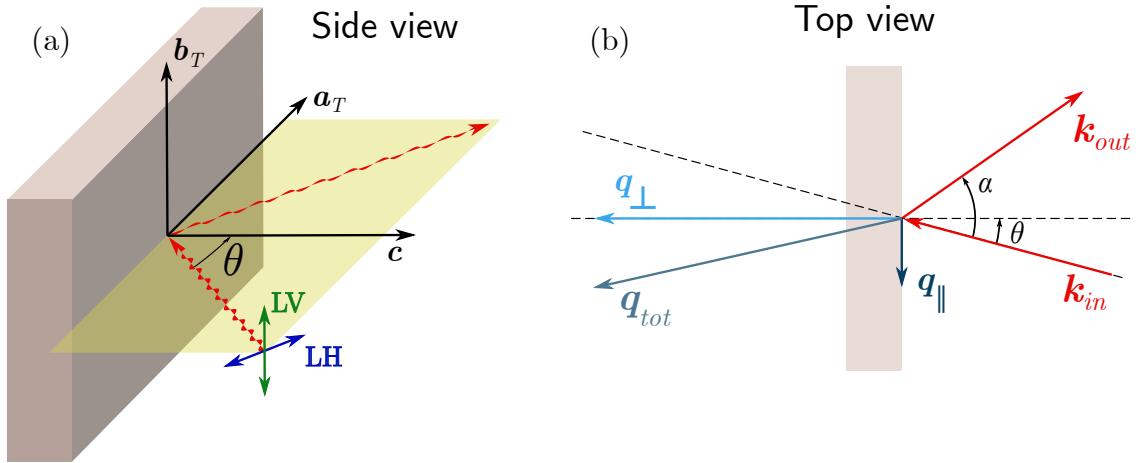


Figure 2.6.: Experimental geometry and momentum transfer. (a) For both XAS and RIXS measurements, the incoming photons \mathbf{k}_{in} have an angle θ with respect to the surface normal and their polarization is either linear vertical (LV, out of scattering plane) or linear horizontal (LH, in the scattering plane). (b) For RIXS measurements, the momentum transferred to the sample $\mathbf{q}_{tot} = \mathbf{k}_{out} - \mathbf{k}_{in}$ can be divided into a component parallel and perpendicular to the surface (Here, $-\mathbf{q}_{tot}$ is plotted for clarity). The angle α between the incoming and outgoing photons is fixed by the experimental setup.

Momentum Transfer

Due to the momentum conservation in the RIXS process, the momentum that is transferred to excitations inside the sample can be calculated from the experimental geometry. Fig. 2.6 shows the geometry of the incoming and outgoing photon with respect to the sample. In the experiments shown in this thesis, the in-plane momentum dispersion is measured along the Ru-O instead of the Ru-Ru direction. Therefore the reciprocal space is indexed by $\mathbf{q} = h\mathbf{a}_T^* + k\mathbf{b}_T^* + l\mathbf{c}^*$ where \mathbf{a}_T^* and \mathbf{b}_T^* are the reciprocal vectors of lattice parameters pointing along the in-plane Ru-O bond as in tetragonal convention. The lattice parameters in real space are then $a_T \approx b_T \approx \sqrt{a^2 + b^2}/2 = 3.86 \text{ \AA}$.

The angle θ between the incoming beam and the surface normal is varied during the experiment to change the in-plane momentum transfer along \mathbf{a}_T . The scattering angle between incident and scattered light is fixed by the experimental setup to 130° which leads to $\alpha = 50^\circ$. For the calculation it is assumed that $k_{in} \approx k_{out}$ (elastic case), which introduces a negligible error since an energy difference of a few eV only changes the photon momentum by several 10^{-3} \AA^{-1} from a total momentum in the order of 10^{-1} \AA^{-1} for soft x-rays. Taking into account all the above the in-plane

momentum is calculated as

$$\begin{aligned}
|\mathbf{q}_{tot}| &= |\mathbf{k}_{out} - \mathbf{k}_{in}| = 2k_{in} \cos(\alpha/2) \\
q_{\parallel} &= |\mathbf{q}_{tot}| \sin(\alpha/2 - \theta) \\
q_{\perp} &= |\mathbf{q}_{tot}| \cos(\alpha/2 - \theta) \\
h &= \frac{q_{\parallel}}{2\pi/a_T}
\end{aligned} \tag{2.1}$$

2.2.4. Second Order Perturbation Scattering Theory

This section covers the theory behind RIXS and the derivation of the RIXS cross section, following closely the derivation found in the review of Ament *et al.* [28].

In the RIXS process, a photon hits the sample and resonantly excites the electrons inside the material. After this, part of the absorbed energy is released by emitting another photon. The theoretical description of this process therefore includes the electrons, the electromagnetic field of the photon and the interaction terms. To tackle this complex problem, it is common to start from the electrons without electromagnetic potentials and then add the interaction in a perturbative way. To this end, we start by writing down the complete Hamiltonian that describes the problem and then separate the part H' describing the electron-photon interaction from the remaining terms H_0 , which describe the electron and photon in the absence of interaction. H' can then be treated as a perturbation to H_0 and the Fermi's golden rule up to second order will describe the transition rate for the RIXS process, leading to the RIXS cross section.

To start, the system containing a set of N electrons in interaction with an electromagnetic field is described by the following Hamiltonian:

$$\begin{aligned}
H &= \sum_{i=1}^N \left(\frac{[\mathbf{p}_i + e\mathbf{A}(\mathbf{r}_i)]^2}{2m} + \frac{e\hbar}{2m} \boldsymbol{\sigma}_i \cdot \mathbf{B}(\mathbf{r}_i) \right. \\
&\quad \left. + \frac{e\hbar}{2(2mc)^2} \boldsymbol{\sigma}_i \cdot \{ \mathbf{E}(\mathbf{r}_i) \times [\mathbf{p}_i + e\mathbf{A}(\mathbf{r}_i)] - [\mathbf{p}_i + e\mathbf{A}(\mathbf{r}_i)] \times \mathbf{E}(\mathbf{r}_i) \} \right) \\
&\quad + H_{Coulomb} + \sum_{\mathbf{k}, \epsilon} \hbar\omega_{\mathbf{k}} \left(a_{\mathbf{k}\epsilon}^{\dagger} a_{\mathbf{k}\epsilon} + \frac{1}{2} \right),
\end{aligned} \tag{2.2}$$

where the electron i has momentum and position operators \mathbf{p}_i and \mathbf{r}_i and Pauli matrices $\boldsymbol{\sigma}_i$ acting on it. $\mathbf{A}(\mathbf{r}, t)$ is the vector potential of the incoming x-rays, defining the electric field $\mathbf{E}(\mathbf{r}) = -\nabla\phi - \partial\mathbf{A}/\partial t$ and the magnetic field $\mathbf{B}(\mathbf{r}) = \nabla \times \mathbf{A}$. The creation (annihilation) of the photon with wave vector \mathbf{k} and polarization ϵ is

represented by the operators $a_{\mathbf{k}\epsilon}^\dagger$ ($a_{\mathbf{k}\epsilon}$). The vector potential can be expanded in plane waves to

$$\mathbf{A}(\mathbf{r}) = \sum_{\mathbf{k}, \epsilon} \sqrt{\frac{\hbar}{2V\epsilon_0\omega_{\mathbf{k}}}} \left(\epsilon a_{\mathbf{k}\epsilon} e^{i\mathbf{k}\cdot\mathbf{r}} + \epsilon^* a_{\mathbf{k}\epsilon}^\dagger e^{-i\mathbf{k}\cdot\mathbf{r}} \right), \quad (2.3)$$

where V is the volume of the system.

In the Hamiltonian, Eq. (2.2), the first term represents the kinetic energy of the electron in the presence of an electromagnetic field. The second term yields the Zeeman splitting, and the third describes the spin-orbit coupling. $H_{Coulomb}$ contains the remaining electrostatic contributions, as the interaction of electrons with an external electric potential and with other electrons and nuclei in the sample. The last term is the energy of the radiation summed over all modes.

Now we split the Hamiltonian H into the electron-photon interaction part H' and the remaining terms H_0 . All terms in H that are independent of \mathbf{A} are included in H_0 , while the others contribute to H' . However, the terms linear in \mathbf{A} coming from the third term of Eq. (2.2) are neglected because this derivation is done in two limits: one of the electron's speed v being small compared to the speed of light (non-relativistic), and the other of small potentials compared to twice the mass of the electron ($e\phi/2mc^2, e|\mathbf{A}|/2mc \ll 1$). Additionally, these terms would only contribute to the second order term in the transition rate as we will see below. Fixing the gauge by choosing $\nabla \cdot \mathbf{A}(\mathbf{r}) = 0$ so that $\mathbf{A} \cdot \mathbf{p} = \mathbf{p} \cdot \mathbf{A}$ we have for H' :

$$H' = \sum_{i=1}^N \left[\frac{e}{m} \mathbf{A}(\mathbf{r}_i) \cdot \mathbf{p}_i + \frac{e^2}{2m} \mathbf{A}^2(\mathbf{r}_i) + \frac{e\hbar}{2m} \boldsymbol{\sigma}_i \cdot \nabla \times \mathbf{A}(\mathbf{r}_i) - \frac{e^2\hbar}{(2mc)^2} \boldsymbol{\sigma}_i \cdot \frac{\partial \mathbf{A}(\mathbf{r}_i)}{\partial t} \times \mathbf{A}(\mathbf{r}_i) \right]. \quad (2.4)$$

To calculate the transition rate for the RIXS process, it is assumed that there is a single initial photon with energy $\hbar\omega_{\mathbf{k}}$ and polarization ϵ that is scattered to energy $\hbar\omega_{\mathbf{k}'}$ and polarization ϵ' in the final state. Due to the scattering with the photon, the electron system in the material changes from the ground state $|g\rangle$ to the final state $|f\rangle$ with energies E_g and E_f . In the process, the photon transfers momentum $\hbar\mathbf{q} = \hbar(\mathbf{k} - \mathbf{k}')$ and energy $\hbar\omega = \hbar(\omega_{\mathbf{k}} - \omega_{\mathbf{k}'})$ to the material. Using the Fermi's golden rule to second order, the transition rate can now be calculated. The second order term is needed because we look at a resonant process where the photon promotes the electron in a first step to an excited intermediate state before it relaxes into the final state. This leads to:

$$w = \frac{2\pi}{\hbar} \sum_{f, \mathbf{k}', \epsilon'} \left| \langle f; \mathbf{k}' \epsilon' | H' | g; \mathbf{k} \epsilon \rangle + \sum_n \frac{\langle f; \mathbf{k}' \epsilon' | H' | n \rangle \langle n | H' | g; \mathbf{k} \epsilon \rangle}{E_g + \hbar\omega_{\mathbf{k}} - E_n} \right|^2 \cdot \delta(E_f + \hbar\omega_{\mathbf{k}'} - E_g - \hbar\omega_{\mathbf{k}}). \quad (2.5)$$

Here, the first order direct transition from initial to final state describes the non-resonant inelastic scattering which generally dominates over the second order. But if the incoming x-rays are in resonance with a transition in the material ($\hbar\omega_{\mathbf{k}} \approx E_n - E_g$), the second order term which describes resonant inelastic scattering becomes large.

Having a closer look at the terms in H' and Eq. (2.5), one can classify H' into terms linear and quadratic in \mathbf{A} . The quadratic ones contain terms of the form $a_{\mathbf{k}'\epsilon'}^\dagger a_{\mathbf{k}\epsilon}$ and $a_{\mathbf{k}\epsilon} a_{\mathbf{k}'\epsilon'}^\dagger$, hence they are the only ones contributing to the first order term as they include annihilation and creation of a photon in one step and give rise to non-resonant scattering. In principle, these terms would also appear in the second order, but there they are neglected because they are comparatively small [28].

Altogether, only two terms contribute to the first order amplitude, the one proportional to \mathbf{A}^2 and the $\boldsymbol{\sigma}_i \cdot \frac{\partial \mathbf{A}}{\partial t} \times \mathbf{A}$ term. The latter is much smaller and is therefore neglected as well. The first order term is then given by

$$\frac{e^2}{2m} \left\langle f; \mathbf{k}' \epsilon' \left| \sum_i \mathbf{A}^2(\mathbf{r}_i) \right| g; \mathbf{k} \epsilon \right\rangle = \frac{\hbar e^2}{2mV\epsilon_0} \frac{\boldsymbol{\epsilon}'^* \cdot \boldsymbol{\epsilon}}{\sqrt{\omega_{\mathbf{k}} \omega_{\mathbf{k}'}}} \left\langle f; \mathbf{k}' \epsilon' \left| \sum_i e^{i\mathbf{q} \cdot \mathbf{r}_i} \right| g; \mathbf{k} \epsilon \right\rangle. \quad (2.6)$$

As mentioned above, this term is dominating when the incident photon energy $\hbar\omega_{\mathbf{k}}$ is far away from any resonance. In the case of hard x-rays and zero energy transfer, this term contributes among others to the Bragg peaks. In the following the first order term will be omitted because RIXS spectra show a strong resonance behaviour which demonstrates that for these processes the second order term is dominating.

The second order amplitude in Eq. (2.5) includes then only the two resonant terms linear in \mathbf{A} of Eq. (2.4): the nonmagnetic term $\mathbf{A} \cdot \mathbf{p}$ and the magnetic $\boldsymbol{\sigma} \cdot \nabla \times \mathbf{A}$ term. Again it can be shown from an estimate that the nonmagnetic term dominates [28]. The magnetic term is therefore ignored and the remaining relevant operator for the resonant transition becomes

$$\mathcal{D} = \frac{1}{im\omega_{\mathbf{k}}} \sum_{i=1}^N e^{i\mathbf{k}\mathbf{r}_i} \boldsymbol{\epsilon} \cdot \mathbf{p}_i, \quad (2.7)$$

where the prefactor has been chosen to simplify the expressions that follow.

Finally the double-differential cross section $I(\omega, \mathbf{k}, \mathbf{k}', \boldsymbol{\epsilon}, \boldsymbol{\epsilon}')$ can be obtained by inserting the relevant parts of H' for resonant scattering in the second order term of Eq. (2.5), multiplying the density of photon states in the solid angle $d\Omega$: $\rho = V\mathbf{k}'^2 d|\mathbf{k}'| d\Omega / (2\pi)^3$ and dividing by the incident flux c/V [38]. The resulting **Kramers-Heisenberg** equations are

$$I(\omega, \mathbf{k}, \mathbf{k}', \boldsymbol{\epsilon}, \boldsymbol{\epsilon}') = r_e^2 m^2 \omega_{\mathbf{k}'}^3 \omega_{\mathbf{k}} \sum_f |\mathcal{F}_{fg}(\mathbf{k}, \mathbf{k}', \boldsymbol{\epsilon}, \boldsymbol{\epsilon}', \omega_{\mathbf{k}}, \omega_{\mathbf{k}'})|^2 \delta(E_g - E_f + \hbar\omega) \quad (2.8)$$

$$\mathcal{F}_{fg}(\mathbf{k}, \mathbf{k}', \boldsymbol{\epsilon}, \boldsymbol{\epsilon}', \omega_{\mathbf{k}}, \omega_{\mathbf{k}'}) = \sum_n \frac{\langle f | \mathcal{D}'^\dagger | n \rangle \langle n | \mathcal{D} | g \rangle}{E_g + \hbar\omega_{\mathbf{k}} - E_n + i\Gamma_n}, \quad (2.9)$$

where the classical electron radius $r_e = (1/4\pi\epsilon_0)e^2/mc^2$ and the prime in \mathcal{D}' refers to transitions related to the outgoing x-rays. In the scattering amplitude \mathcal{F}_{fg} a lifetime broadening Γ_n is introduced for the intermediate states n . This accounts for the nonradiative interaction terms like Auger decay that are not included in H' and make the intermediate states short lived.

From the Kramers-Heisenberg equations Eq. (2.8) and Eq. (2.9) one can make different approaches to proceed. In a next step one can separate the scattering amplitude $\mathcal{F}_{fg}(\mathbf{k}, \mathbf{k}', \boldsymbol{\epsilon}, \boldsymbol{\epsilon}', \omega_{\mathbf{k}}, \omega_{\mathbf{k}'})$ into two parts: one includes the geometry of the experiment coming from the photon momentum and polarization vectors and the other is the fundamental scattering amplitude that relates to the physical properties of the system under study. This separation can be done exactly and leads to

$$\mathcal{F}_{fg}(\mathbf{k}, \mathbf{k}', \boldsymbol{\epsilon}, \boldsymbol{\epsilon}', \omega_{\mathbf{k}}) = \sum_x \mathbf{T}^x(\hat{\mathbf{k}}, \hat{\mathbf{k}}', \boldsymbol{\epsilon}, \boldsymbol{\epsilon}') \cdot \mathbf{F}^x(k, k', \omega_{\mathbf{k}}), \quad (2.10)$$

with the fundamental scattering amplitude $\mathbf{F}^x(k, k', \omega_{\mathbf{k}})$ and the angular dependence $\mathbf{T}^x(\hat{\mathbf{k}}, \hat{\mathbf{k}}', \boldsymbol{\epsilon}, \boldsymbol{\epsilon}')$. Hence the RIXS scattering amplitude is a linear combination of these fundamental scattering amplitudes weighted by the angular functions $\mathbf{T}^x(\hat{\mathbf{k}}, \hat{\mathbf{k}}', \boldsymbol{\epsilon}, \boldsymbol{\epsilon}')$. To understand the fundamental scattering amplitudes and compute the exact RIXS response of a material is very demanding and sometimes a virtually impossible task. However, different approaches can be divided in numerical and approximative evaluations. One method is to evaluate the exact scattering amplitude and RIXS intensity numerically, but for a simplified system like in an effective single-particle description or small cluster of atoms. A complementary approach is to use an approximation for the interactions of the system with the intermediate core-hole to obtain an effective theory. The best way to come to an effective solution depends strongly on the system and the RIXS process that is investigated.

2.3. Sample Preparation

Before the experiment, the single crystals were aligned *ex-situ* with a Laue x-ray diffractometer to orient the crystallographic axes. A polychromatic x-ray beam is focused on the sample and the backscattered signal is detected by a two-dimensional screen. Since the incident beam contains different wavelengths, several crystal planes fulfil the Bragg condition and multiple peaks are visible. By rotating the crystal, one can identify high-symmetry planes and the crystal axes. Fig. 2.7 (a) shows the diffraction pattern of $\text{Ca}_3\text{Ru}_2\text{O}_7$ in the *ab*-plane that is typical for perovskite

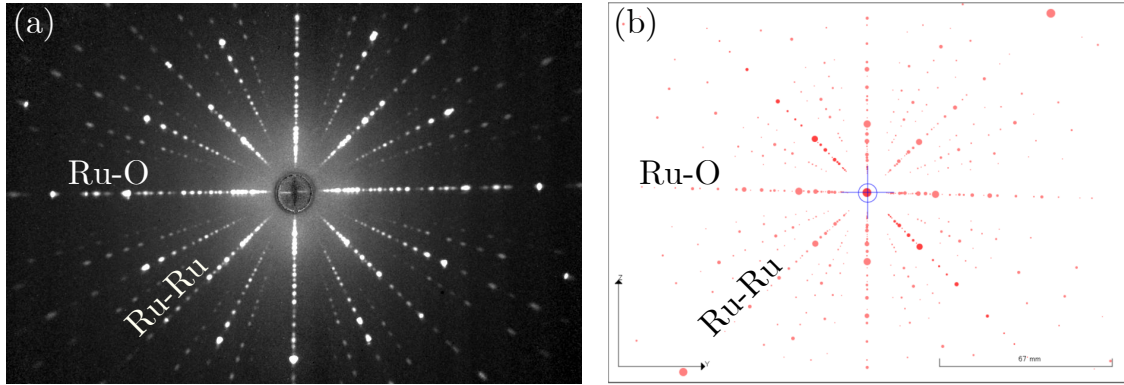


Figure 2.7.: (a) Measured Laue pattern of $\text{Ca}_3\text{Ru}_2\text{O}_7$. Adapted from Ref. [39] (b) Corresponding simulated Laue pattern. The crystal bonds in the measured pattern can be assigned according to the indicated directions in the simulated pattern.

structured materials. The different axes along Ru-O and Ru-Ru, standing at an angle of 45° to each other, can be identified thanks to higher-order reflections. These are closer to the Ru-Ru bond directions. This is also verified by comparison to the simulated Laue pattern in Fig. 2.7 (b). In this way, the sample was aligned such that the c -axis is perpendicular to the surface and Ru-O and Ru-Ru directions were marked to allow later RIXS measurements along the Ru-O direction.

For the experiments presented in this thesis, a low surface roughness is important for a good data quality. This has two reasons: first, the soft x-rays have a shorter penetration depth. Second, RIXS is a very photon hungry technique and diffuse scattering on the surface should therefore be minimised. In order to obtain a clean and flat surface, the sample was cleaved *in-situ* at base temperature and high vacuum with the standard top-post procedure.

3. Results

In this chapter, results on the bilayer $\text{Ca}_3\text{Ru}_2\text{O}_7$ are presented and compared to recent studies of the single layer Ca_2RuO_4 [40, 41]. The first section focuses on the XAS and the second on the RIXS measurements. At the ADRESS beamline, both experiments are done within the same measurement chamber by simply switching the detectors from diodes for the XAS experiment to the SAXES spectrometer for RIXS.

3.1. XAS Measurements

Before the low energy excitation spectrum can be measured by RIXS, the energy of the incoming photon beam is tuned to an absorption edge in the material under investigation. Because the exact energy difference between occupied and unoccupied levels is material and site dependent, the exact fine structure of the edge is first determined by a XAS measurement. The absorption spectrum already reveals a lot of desirable information about the structure of the sample. In this chapter, it is shown how the different sites of the oxygen in the $\text{Ca}_3\text{Ru}_2\text{O}_7$ crystal result in distinguishable absorption energies and that the coupling to different Ru d orbitals induces an extra shift in energy. The results on $\text{Ca}_3\text{Ru}_2\text{O}_7$ are compared to the spectrum taken from Ca_2RuO_4 .

3.1.1. Absorption Edge and Orbital Selectivity

Most of the intriguing physics of the ruthenates evolves from the valence electrons in the moderately localized d shells. The $4d$ shell in the ruthenates is only partially filled because the ground state electron configuration of Ru changes from $[\text{Kr}]4d^75s^1$ to $[\text{Kr}]4d^45s^0$ due to the oxygen octahedron environment. For a complete understanding of the exotic phenomena in these materials it is therefore ideal to look directly at the electronic structure of the d orbitals. However, the Ru $L_{2,3}$ -edges that probe transitions from $2p \rightarrow 4d$ have an energy of $\sim 2.8\text{--}3$ keV which lies in the tender x-ray regime [42]. From a technical point of view, light with this energy causes difficulties

because its wavelength is too large to match the inter-plane spacing in hard x-ray crystal monochromators and too small for the groove of grating monochromators used for soft x-rays. For this reason, there were no instruments available to measure this edge with high energy resolution when the experiments presented in this thesis were done. But it has to be mentioned that just recently a tender x-ray RIXS beamline at PETRA-III operating in the tender x-ray regime has been built. Its spectrometer was especially designed for measuring the L -absorption edges of $4d$ metal compounds and first papers on ruthenates have already been published [43, 44]. However, the energy resolution of this instrument is around 150 meV which is much worse than the resolution that can be obtained with soft x-ray instruments (see section 2.2). The next higher edges are Ru $M_{2,3}$ that probe transitions from $3p \rightarrow 4d$. Though they have an energy in the soft x-ray regime, these edges have been little studied and the ease of measurement is not well established. In fact, the RIXS intensity is currently too small to obtain reasonable data. Another way around the technical obstacles is accessing the Ru d orbitals indirectly through their hybridization with the O p orbitals [40, 41]. The oxygen K -edge is around 530 eV and can be measured with soft x-ray instruments.

Measuring at the oxygen K -edge also allows the experiment to be orbital selective. This is due to the fact that the absorption is determined by the dipole matrix element of O $1s-2p_{x,y,z}$ transitions and the hybridization strength between O $2p_{x,y,z}$ -Ru $4d$ orbitals. The matrix element is fully determined by the relative orientation of the polarization vector and the final state p orbitals because of the initial state s orbital's isotropy. This means that if the polarization vector is aligned with the p orbital direction x, y or z , the transition is enhanced. This procedure has already been applied for different materials like the iridates and is explained in Ref. [45]. In the geometry used for the experiments in this thesis (see Fig. 3.1 (a)) the O p orbitals are aligned along the x, y or z -direction. The incoming light beam lies in the xz -plane with varying angle θ to the z -axis. Therefore, incoming linear vertical (LV) light has the polarization out of the scattering plane along the y -direction and interacts predominantly with p_y orbitals. For linear horizontal (LH) polarized light the polarization vector lies in the scattering plane and points either along the x -direction for normal incidence ($\theta = 0^\circ$) or along the z -direction for near grazing incidence. Thus, this light polarization probes the changeover from in-plane p_x orbitals to out-of-plane p_z orbitals. Changing the light polarization and varying the incident angle θ therefore makes it possible to selectively enhance transitions to specific p orbitals.

Fig. 3.1 (b)-(d) illustrate how the different p orbitals from planar or apical oxygen sites hybridize with the different Ru $4d$ orbitals. Taking all these considerations together, one can for example infer that for measurements with LV polarization which

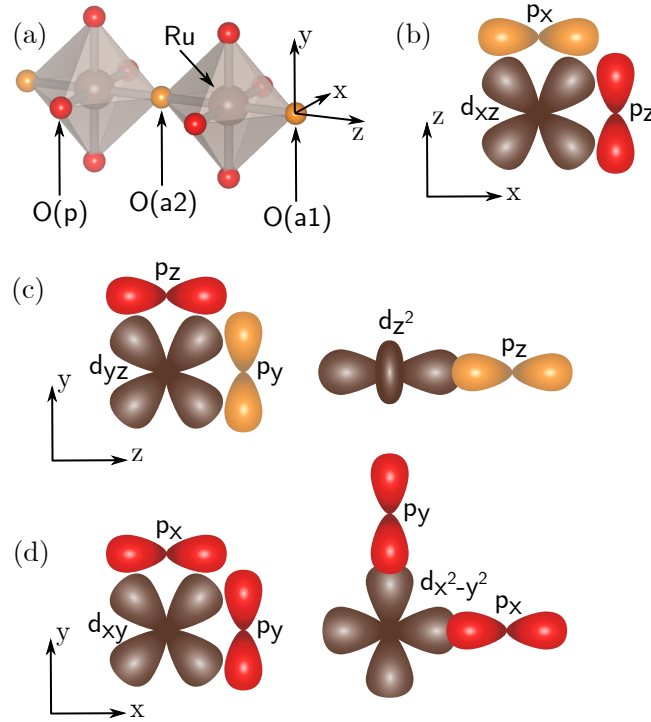


Figure 3.1.: (a) Simplified crystal structure without calcium atoms. The orange apical oxygen atoms lie on the out-of-plane crystal c -axis whereas the red planar oxygen atoms are on the ab crystal plane. Incoming light lies in the xz -plane with a varying angle θ to the z -axis (compare Fig. 2.6) (b)-(d) Illustration of the O $2p$ - Ru $4d$ hybridization. Red and orange p orbitals correspond to planar and apical oxygen sites, respectively.

aligns the electrical field with p_y orbitals, the apical oxygen absorption probes the occupancy of Ru d_{yz} while the absorption on planar oxygen probes the Ru d_{xy} and $d_{x^2-y^2}$ through hybridization with the oxygen p_y orbital. Table 3.1 shows a summary of the orbital selectivity achieved by different experimental conditions. The orbitals written in bold correspond to the t_{2g} states which are lower in energy than the e_g states. Because of this, the peaks in an absorption spectra corresponding to these orbitals will also be at lower energies. The apical and planar absorption edges of the oxygen can generally be distinguished through their energy as well. Because they experience a different chemical environment, the absorption resonances are changed. In single layered ruthenates this difference is around 1 eV. However, for bilayered structures there are two different apical sites where only one of them, the O(a1) has just one ruthenium neighbour. The apical oxygen O(a2) in the middle of the two layers is in between two ruthenium atoms and its chemical environment is therefore more close to the one of planar oxygen. This difference will manifest itself in the absorption spectra presented in the next section.

| | | Apical O | Planar O |
|------------|-------|-------------------|------------------------------------|
| LH normal | p_x | $\mathbf{d_{xz}}$ | $\mathbf{d_{xy}}, d_{x^2-y^2}$ |
| LH grazing | p_z | d_{z^2} | $\mathbf{d_{xz}}, \mathbf{d_{yz}}$ |
| LV | p_y | $\mathbf{d_{yz}}$ | $\mathbf{d_{xy}}, d_{x^2-y^2}$ |

Table 3.1.: Summary of the different experimental conditions that enhance transitions from planar or apical oxygen into certain Ru d orbitals. Orbitals in bold correspond to t_{2g} states at lower energy.

3.1.2. Absorption Spectra of $\text{Ca}_3\text{Ru}_2\text{O}_7$

Fig. 3.2 shows the oxygen K -edge absorption spectra of $\text{Ca}_3\text{Ru}_2\text{O}_7$ recorded in total fluorescence yield at base temperature $T = 23$ K. It compares measurements taken with LH or LV polarization for normal ($\theta = 0^\circ$) and near grazing ($\theta = 74^\circ$) light incidence. A constant background was subtracted and the spectra were normalized to the maximum intensity. The same data processing procedure was applied to all XAS spectra of $\text{Ca}_3\text{Ru}_2\text{O}_7$ shown in this thesis. The first striking feature of the spectra in Fig. 3.2 is the similarity between both LV and the LH spectrum at normal incidence: they are completely identical in the near-edge region at lower energies. The absence of a dependence on the incident angle in the LV spectra is consistent with the assumption that always the same orbitals are probed with this polarization. However, the similarity between LV and LH normal incidence spectra confirms that the hybridization between the two in-plane O p_x/p_y and the Ru d_{xz}/d_{yz} orbitals is indistinguishable. This reflects that the x and y direction in the crystal are almost equivalent. Furthermore, it is a strong indication that a splitting in energy between the d_{xz} and d_{yz} orbitals has to be much smaller than the energy resolution of this experiment ($\sim 15 - 35$ meV at oxygen K -edge [31]).

The situation looks different for LH polarization at grazing incidence. There we are probing the out-of-plane p_z orbital that is hybridizing with the two t_{2g} orbitals d_{xz}, d_{yz} . Through the apical oxygen site we are only sensitive to the e_g orbital d_{z^2} which lies at higher energies. Comparing the low energy part of the spectrum, the shoulder at around 528.3 eV in the LV and LH normal incidence spectra (indicated by a dashed vertical line) is clearly gone for LH grazing incidence. This leads to the conclusion that this lowest energy peak can be assigned to the apical resonance probing d_{xz} and d_{yz} . In fact, it is a common feature for single layer perovskite structured TMO's that the apical resonance is at 1-2 eV lower energies than the planar one. This is observed for Ca_2RuO_4 [46], strontium ruthenates [47], iridates [45] and cuprates [48]. The same trend can be observed in our data for the bilayer $\text{Ca}_3\text{Ru}_2\text{O}_7$, although the difference in energy to the pronounced peak around 528.9 eV seems to be less than 1 eV.

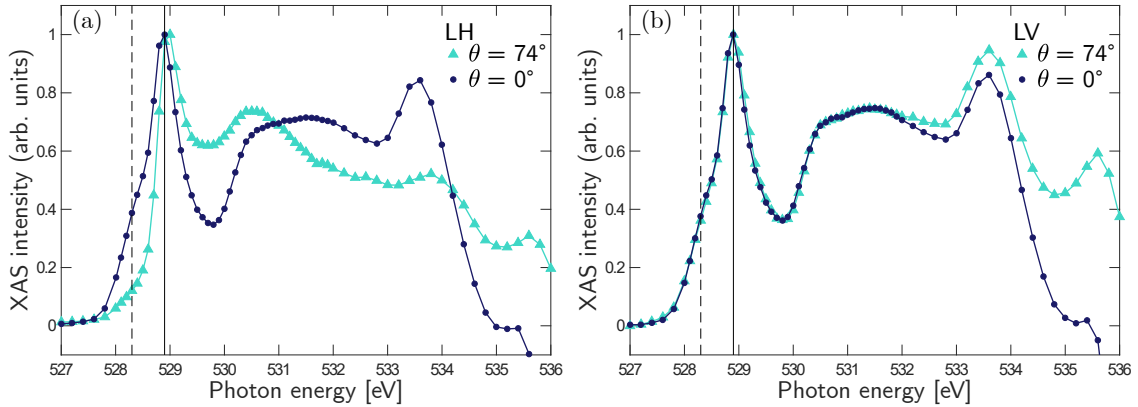


Figure 3.2.: Oxygen K -edge XAS for (a) LH polarized and (b) LV polarized light recorded at $T = 23$ K. $\theta = 0^\circ$ corresponds to normal incidence of the incoming photon beam and $\theta = 74^\circ$ is near grazing incidence.

Common to all spectra is the strong peak at 528.9 eV (indicated by a solid vertical line). Only for LH polarized light at grazing incidence this resonance is shifted slightly to 529 eV. On one hand this peak can be assigned to the planar oxygen site hybridizing with t_{2g} ruthenium orbitals. On the other hand, considering the two different apical sites O(a1) and O(a2) in $\text{Ca}_3\text{Ru}_2\text{O}_7$, they have a significantly different chemical environment and should therefore have distinguishable absorption energies. Thus, the spectra shown here suggest that the inner apical O(a2) and planar site O(p) are very close in energy so that the strong peak is arising from these two sites. The resonances at higher energies stem from hybridization of the O p orbitals with the Ru e_g states. However, at higher energy the spectra do not allow for an unambiguous assignment of the peaks to certain resonances. To be more specific, it is not possible to distinguish resonances from apical or planar sites hybridized with the two e_g states $d_{x^2-y^2}$, d_{z^2} .

In summary, we have assigned the lowest energy contribution at 528.3 eV to come from O(a1)- t_{2g} hybridization and the strong peak at 528.9 eV to have O(p)/O(a2)- t_{2g} character. For brevity and clarity the features are from now on relabelled to apical for the former resonance and planar for the latter. However, it should be kept in mind that the planar resonance has contributions from both O(p) and O(a2).

Fig. 3.3 (a) shows the temperature dependence between the base temperature $T = 23$ K up to $T = 79$ K of the LV spectra at normal incidence. It is clearly seen that there is no significant dependence of the absorption on temperature. Both the energy as well as the relative intensity of the different resonances stay exactly the same. This is remarkable considering the major changes $\text{Ca}_3\text{Ru}_2\text{O}_7$ undergoes both electronically and magnetically between these temperatures. As introduced in section

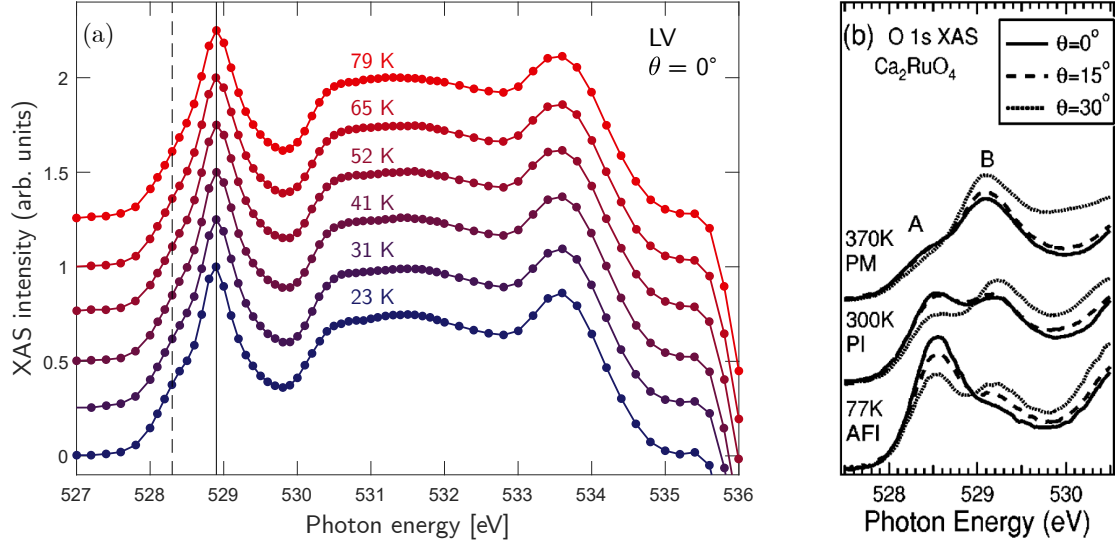


Figure 3.3.: (a) Temperature dependence of the $\text{Ca}_3\text{Ru}_2\text{O}_7$ oxygen K -edge XAS taken with LV polarized light at normal incidence. The spectra are normalized and shifted vertically for clarity. (b) Temperature and angle dependence for Ca_2RuO_4 . A and B label the apical and planar feature, respectively. Taken from Ref. [49].

1.2.2, $\text{Ca}_3\text{Ru}_2\text{O}_7$ undergoes two phase transitions when it is cooled. First a magnetic transition at $T_N = 56$ K where the material enters an A-type AFM state and then a structural transition at $T_s = 48$ K. Below this temperature, the out-of-plane resistivity has a sharp increase while the in-plane resistivity decreases with lowering temperature. This leaves the system in a poorly metallic antiferromagnetic state. However, none of these changes in macroscopic observables seem to be showing up in the absorption measurement. In contrast, Ca_2RuO_4 shows dramatic changes going through the structural transition at $T_s = 356$ K and the magnetic transition at $T_N = 110$ K as can be seen in Fig. 3.3 (b). There, the relative intensity of apical and planar resonances (labelled A and B, respectively) switches by going from a paramagnetic metal to an antiferromagnetic insulator.

It has to be mentioned that even though only one spectrum (LV, $\theta = 0^\circ$) is shown for $\text{Ca}_3\text{Ru}_2\text{O}_7$ in this thesis, all four different experimental conditions (LH/LV, $\theta = 0^\circ/74^\circ$) were measured temperature dependent. For all conditions, the spectrum does not change at all when the temperature is raised up to $T = 79$ K.

3.1.3. Comparison to Ca_2RuO_4

The structural and magnetic differences between the single layer Ca_2RuO_4 and the bilayer $\text{Ca}_3\text{Ru}_2\text{O}_7$ are well reflected in the absorption spectra. Fig. 3.4 (a) compares

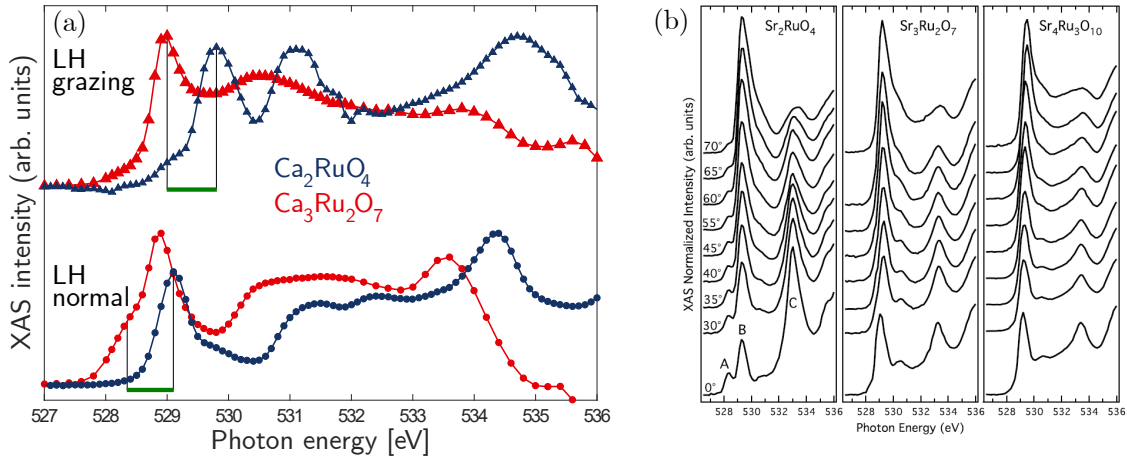


Figure 3.4.: (a) XAS comparison of $\text{Ca}_3\text{Ru}_2\text{O}_7$ data with Ca_2RuO_4 data from Ref. [41]. Green bars indicate energy difference between the apical resonances in the lower panel and between the planar resonances in the upper panel. (b) XAS spectra at oxygen K -edge for strontium ruthenates. Taken from Ref. [47].

the spectra of $\text{Ca}_3\text{Ru}_2\text{O}_7$ from Fig. 3.2 (a) with spectra of Ca_2RuO_4 recorded under the same experimental conditions that were published recently in Ref. [41].

In the single layer Ca_2RuO_4 , the ruthenium atom is also surrounded by an oxygen octahedron and we have the same orbital selectivity for the different experimental conditions as displayed in table 3.1. But for Ca_2RuO_4 it is known that the t_{2g} triplet is not degenerate. The c -axis compression at the structural transition lowers the energy of the d_{xy} band and leaves it almost completely occupied. This orbital is therefore not accessible in the XAS process and can not be probed. Another difference is that there is only one layer of the perovskite lattice alternating with spacer layers. This means that the oxygen can only occupy two different sites in the crystal: either the apical at the border to the spacer layer or the planar site within the Ru-O plane.

The dark blue spectrum of Ca_2RuO_4 in the lower half of Fig. 3.4 (a) was recorded with LH polarization at normal incidence. This experimental condition measures the p_x orbital hybridized with d_{xz} at the apical site and with $d_{x^2-y^2}$ at the planar site. In good agreement with this there is only one strong peak in the low energy part which has apical t_{2g} character. In the upper half of Fig. 3.4 (a), the spectrum for grazing incidence is shown. In this condition, the orbitals probed are d_{xz}/d_{yz} at the planar site and the high energy d_{z^2} at the apical site. As expected, the apical t_{2g} peak is strongly suppressed here and instead a pronounced response is observed at slightly higher energy having planar t_{2g} character.

Comparing $\text{Ca}_3\text{Ru}_2\text{O}_7$ and Ca_2RuO_4 spectra, it can be observed that the whole

$\text{Ca}_3\text{Ru}_2\text{O}_7$ spectrum is shifted consistently to lower energies as indicated by green bars for the apical and planar resonance. The extracted low energy t_{2g} resonances are summarized in table 3.2. They support the observation and reveal a shift value of 0.8 eV. Consistent for both compounds is the separation of the apical and planar resonance by 0.7 eV.

| | $\text{Ca}_3\text{Ru}_2\text{O}_7$ | Ca_2RuO_4 |
|--------|------------------------------------|---------------------------|
| apical | 528.3 eV | 529.1 eV |
| planar | 529.0 eV | 529.8 eV |

Table 3.2.: Energies of the low energy XAS resonances of $\text{Ca}_3\text{Ru}_2\text{O}_7$ and Ca_2RuO_4 . The planar resonance value of $\text{Ca}_3\text{Ru}_2\text{O}_7$ is extracted from the LH grazing spectrum, where the measurement is mainly sensitive to O(p) contributions only at low energies. The data analysis procedure is illustrated in appendix A.

3.1.4. Discussion

The XAS spectra of $\text{Ca}_3\text{Ru}_2\text{O}_7$ reported here can be consistently interpreted with orbital selectivity by light polarization and incident angle as it was applied in previous studies of ruthenates [40, 41]. It seems that the resonance mediated by the inner apical oxygen O(a2) is very close in energy to the planar O(p). Because of this, these two can not be distinguished in the spectra which makes it impossible to draw any direct conclusion about the occupation of the d_{xy} orbital. However, the c -axis compression is much smaller in $\text{Ca}_3\text{Ru}_2\text{O}_7$ than in Ca_2RuO_4 which leads to the assumption of less d_{xy} occupancy in $\text{Ca}_3\text{Ru}_2\text{O}_7$. For Ca_2RuO_4 , the spectra are in perfect accordance with an almost fully occupied d_{xy} orbital and apical and planar resonances can be distinguished easily in the spectra. The fact that the inner apical resonance shifts towards the planar resonance for increasing number of layers has already been seen in the $\text{Sr}_{n+1}\text{Ru}_n\text{O}_{3n+1}$ series [47]. Fig. 3.4 (b) shows XAS spectra at the oxygen K -edge for different incident angles measured on the single layer, bilayer and trilayer compound. There it is also observed that the double apical and planar peak for Sr_2RuO_4 turns into a single peak with a shoulder in $\text{Sr}_3\text{Ru}_2\text{O}_7$ and $\text{Sr}_4\text{Ru}_3\text{O}_{10}$. But what is not observed for the strontium series is the shift of the whole spectrum towards lower energies for the bilayer. This seems to be specific for the calcium compound. Another remarkable observation is the lack of temperature dependence of the XAS spectra for the bilayer. As the material undergoes significant changes in electronic properties, it would be expected to see changes in the partially occupied Ru 4d orbitals. In the single layer Ca_2RuO_4 , the XAS spectra show dramatic changes in the relative intensity of apical and planar

resonances by going through structural and magnetic transitions. A reason for the difference between the single and double layer may lie in the temperature regime and magnitude of the structural transition. In Ca_2RuO_4 , T_s is seven times higher and the compression of the c -axis is ten times larger compared to $\text{Ca}_3\text{Ru}_2\text{O}_7$. Thus the relatively small structural changes in $\text{Ca}_3\text{Ru}_2\text{O}_7$, which are not enough to drive the system fully insulating, are not visible in XAS spectra.

3.2. RIXS Measurements

After the absorption spectrum was recorded, the energy of the incident photon beam is set to an absorption edge and a RIXS measurement is performed. This chapter shows the data of $\text{Ca}_3\text{Ru}_2\text{O}_7$ taken under different experimental conditions and the low energy excitations are discussed. They are then compared to Ca_2RuO_4 measurements from Ref. [41].

Unless otherwise indicated, all the measurements on $\text{Ca}_3\text{Ru}_2\text{O}_7$ presented in this chapter are taken at the planar absorption edge at 528.9 eV. This resonance has $\text{O}(p)/\text{O}(a_2)-t_{2g}$ character and probes mainly the Ru d_{xy} , d_{xz} and d_{yz} orbitals via oxygen atoms within the double layer. Since $\text{Ca}_3\text{Ru}_2\text{O}_7$ is a quasi two dimensional crystal the in-plane momentum transferred by the RIXS process is indexed in tetragonal convention as relative lattice unit h in $(h, 0)$ for measurements along the Ru-O bond (see section 2.2.3).

3.2.1. Excitations in Different Experimental Conditions

Fig. 3.5 shows the RIXS spectra of $\text{Ca}_3\text{Ru}_2\text{O}_7$ taken under different experimental conditions where each panel compares another experimental parameter under otherwise identical conditions. In Fig. 3.5 (a) the spectrum shows the RIXS intensity as a function of energy loss up to 5 eV at base temperature recorded with LV polarized light at near grazing incidence. The dark blue curve was taken with an incident photon energy of 528.9 eV which corresponds to the planar resonance whereas the orange curve was taken at the apical resonance with incident photon energy of 528.3 eV. Both spectra were normalized to the integrated intensity of the most pronounced peak around 3.5 eV. In both spectra, three distinct RIXS excitations, labelled as A, B and dd , can be identified. The highest energy excitation has its maximum at around 3.4 eV energy loss at the planar resonance. At the apical resonance, the peak is shifted downwards to around 3.1 eV. Additionally, the peak is less broad and therefore slightly more intense in the normalized spectrum shown here. Excitations A and B show the opposite trend in both position and width. Peak B is shifted

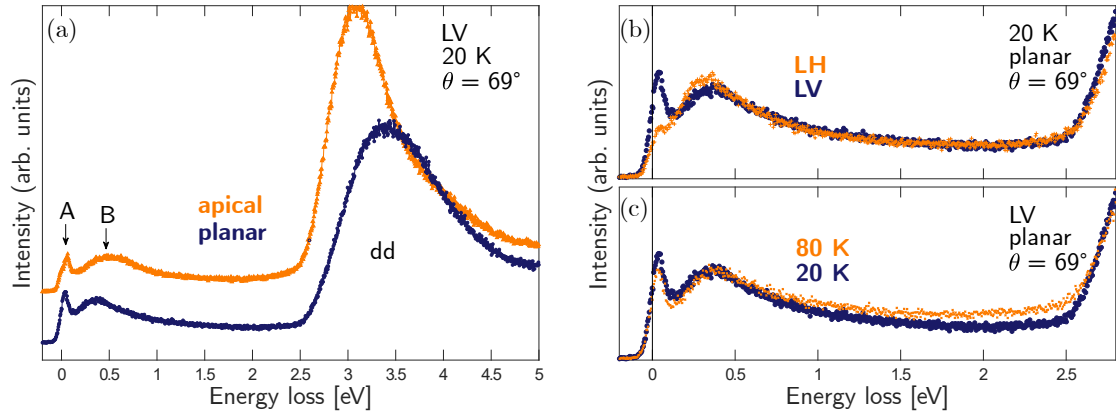


Figure 3.5.: (a) RIXS spectra comparing two different incident energies, one at the apical resonance with $E = 528.3$ eV and the other at the planar resonance with $E = 528.9$ eV. (b) Comparison of the low energy part for different incident light polarizations LV and LH. (c) Comparison for two different temperatures, one below and the other above the structural and magnetic transitions.

towards higher energy loss for the lower incident energy and is much broader. For the A excitation, an unambiguous conclusion is difficult to make since it overlaps strongly with the elastic scattering peak at 0 eV energy loss. However, the two peaks seem to be more separated in the apical curve, indicating that this excitation is also at higher energy loss for lower incident energy. Especially interesting is the intensity behaviour of this lowest energy excitation. In the planar curve it is only apparent as a shoulder on the right side of the elastic peak whereas it appears as a peak with the elastic peak as a shoulder on the left side for the apical curve. This indicates that the A excitation is enhanced for an incident photon energy tuned to the apical resonance which probes Ru d_{xz}/d_{yz} orbitals.

The dependence of the low energy excitations on incident light polarization is shown in panel (b) for incident energy at the planar resonance and base temperature. The dd peak at higher energy, which is not shown in this spectrum, does not show any dependence on light polarization. However, in the low energy part, the elastic scattering at 0 eV energy loss shows a clear difference: it is strongly suppressed for LH polarized light. The reason for this lies in its origin. A large contribution to the elastic peak comes from diffuse scattering due to deformations and crystal defects. Another source is the crystalline surface roughness which also gives rise to diffuse, static scattering. Both contributions are seen in the non-resonant scattering channel which is described by Eq. (2.6). The transition rate for these processes has an $\epsilon' \cdot \epsilon$ polarization dependence, where ϵ' (ϵ) is the scattered (incoming) photon polarization. As a result, non-resonant scattering is minimized for LH polarized light, where the polarization lies in the scattering plane, and for a scattering angle of 90° . This effect

is also seen in the data presented here, where the scattering angle was fixed to 50° . Another difference between the two curves in panel (b) is a slightly more intense B excitation for LH polarization. However, the A and B excitations do not show a strong light polarization dependence, indicating that there is no big difference in exciting into d_{xz}/d_{yz} or d_{xy} orbitals. This further strengthens the assumption that the d_{xy} orbital is not globally fully occupied in the bilayer.

Lastly, two different temperatures are compared in panel (c) of Fig. 3.5. At 20 K, the system is in a poorly metallic and antiferromagnetically ordered state as described in section 1.2.2. The high temperature curve was taken at 80 K, well above the structural and magnetic transition temperatures where the system is a paramagnetic metal. In the previous section it was already seen that the XAS spectrum does not show any temperature dependence between 20 K and 80 K. Consistent with this, the RIXS spectra do not show any distinct changes as well. However, a small enhancement of intensity is observed between approximately 1 eV and 2.5 eV energy loss. The increase in intensity rather has the character of a bigger background than an additional excitation signal. Another small difference in the two spectra is the slightly smaller peak around 0 eV energy loss at 80 K.

In summary, all three excitations (A, B and dd) are measured for all experimental conditions. The dd excitation shows neither a polarization nor a temperature dependence but shifts to lower energy loss for lower incident photon energy. This means that the incident energy does not affect the energy of the re-emitted photon, but rather the amount of energy transferred to the system, suggesting a wide range of final states accessible. Together with the high energy of this excitation this points either towards charge transfer or dd excitations, where the hybridization with broad O p orbitals leads to a relatively broad bandwidth. Comparison to the Ca_2RuO_4 spectrum discussed in section 3.2.3 will allow to assign it to dd excitation. The A and B excitations have no distinct dependence on temperature, indicating that these excitations persist into the paramagnetic regime and therefore do not have a magnetic origin. Whereas the B excitation is slightly enhanced for LH polarization, it is not possible to draw any conclusion for the A excitation as it can not be separated from the extremely weak elastic peak at LH polarization.

Puzzling is the behaviour for these two excitations with varying incident energy. The fact that the B excitation is at higher energy loss for lower incident energy and the considerably broader width could be indications for a different origin.

3.2.2. Momentum Dispersion of Lowest Energy Excitation

In addition to the energy of elementary excitation, RIXS is capable to measure their dependence on momentum by varying the incident angle θ of the photon beam. Even though the angle between incident and scattered light is fixed to 50° for all measurements shown in this thesis keeping also the modulus of momentum fixed, the in-plane component of the momentum transferred to the quasi two-dimensional system can be varied by changing θ . The determination of the in-plane momentum h in relative lattice units from the incident angle θ is explained in detail in section 2.2.3.

To extract the momentum dependence of the lowest energy excitation, LV polarization is chosen. There the elastic peak is pronounced enough to allow for a fit according to the left side of the peak at 0 eV energy loss. The additional weight on the right side of this peak can then be assigned to the A excitation. For the LH spectrum, the weak peak around 0 eV energy loss is overlapping strongly with higher energy components and is not strong enough to be unambiguously divided into two components for the elastic peak and the A excitation. To determine the A excitation energy, the data around 0 eV energy loss is fitted by a 4 component function as described in section 2.2.3 to account for the elastic, A and B peaks and the background. Fig. 3.6 (a) shows two spectra recorded with different incident angles (momentum transfers) as indicated. The solid black line is the Gaussian fit corresponding to the elastic scattering. Here it is clearly evident that this elastic peak with a resolution fixed width is not enough to capture the data below 0.2 eV. As the elastic scattering is most pronounced near specular condition ($\theta = 28^\circ$), the peak in the lower spectrum is dominated by this part and the excitation A is only visible as a shoulder on the right side. Near grazing condition the situation is reversed and the elastic scattering appears as a shoulder on the left side of the excitation peak. In Fig. 3.6 (b), spectra with elastic scattering subtracted according to Gaussian fits as shown in (a) are displayed for different in-plane momentum transfer h to visualize the dispersion of the A excitation. The position of the second Gaussian fit component corresponding to the excitation is indicated with short vertical bars. It is clearly visible that the peak is moving towards lower energy as in-plane momentum is increased.

Even though the B excitation is mimicked by a damped harmonic response function in the fitting, the resulting width of the peak is higher than the energy of the excitation. This indicates that the feature in the spectrum is composed of more than one component. The data presented here do however not allow for a deconvolution of the peak. For this reason, the peak position was extracted from fitting the zero of the peak derivative. This procedure is summarized in appendix B. Within the accuracy of this method and the energy resolution of this experiment, no dispersion

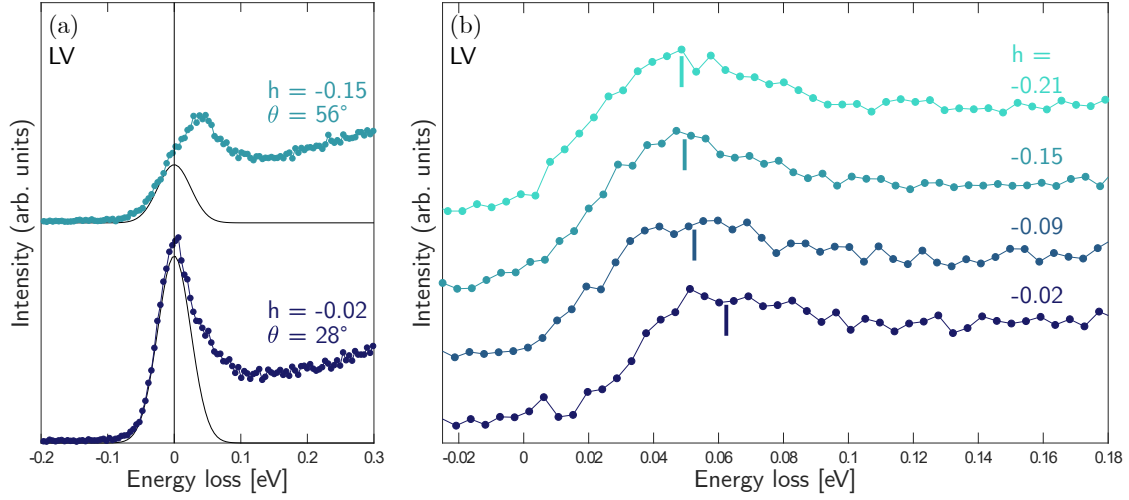


Figure 3.6.: (a) Zoom around the elastic peak for two spectra taken with LV polarization for incident angle (momentum transfer) as indicated. Solid black curves are Gaussian fits of the elastic component. Shoulder to the right of the elastic peak indicate an overlapping low energy excitation. (b) RIXS spectra as a function of in-plane momenta with elastic scattering subtracted according to Gaussian fits as shown in (a). Short vertical bars indicate the position of the Gaussian fit for the low energy excitation.

for the B excitation can be observed. The results of the momentum dependence together with the results of Ca_2RuO_4 are summarized in the next section.

3.2.3. Comparison to Ca_2RuO_4

The results on $\text{Ca}_3\text{Ru}_2\text{O}_7$ are now compared to the single layer Ca_2RuO_4 with focus on distinct differences in the spectra. This allows for a more profound interpretation of the excitations found in $\text{Ca}_3\text{Ru}_2\text{O}_7$, since the low energy features in Ca_2RuO_4 have a strong orbital character and are interpreted as manifestations of the materials band-Mott insulating nature. The differences in RIXS can therefore be discussed in terms of the dissimilar spin and orbital ground states. Fig. 3.7 (a) shows the data on $\text{Ca}_3\text{Ru}_2\text{O}_7$ in red, taken with LH and LV polarized light at incident angle as indicated, as well as data on Ca_2RuO_4 in dark blue from Ref. [41], taken at almost the same experimental conditions.

In Ca_2RuO_4 , four low energy excitations labelled A, B, C and D can be observed with approximate energy losses of 0.08, 0.35, 1.3 and 2.4 eV. The broad and intense peak around 4 eV energy loss corresponds approximately to t_{2g} to e_g splitting in XAS spectra and is hence assigned to dd excitations in Ref. [40]. The intensity

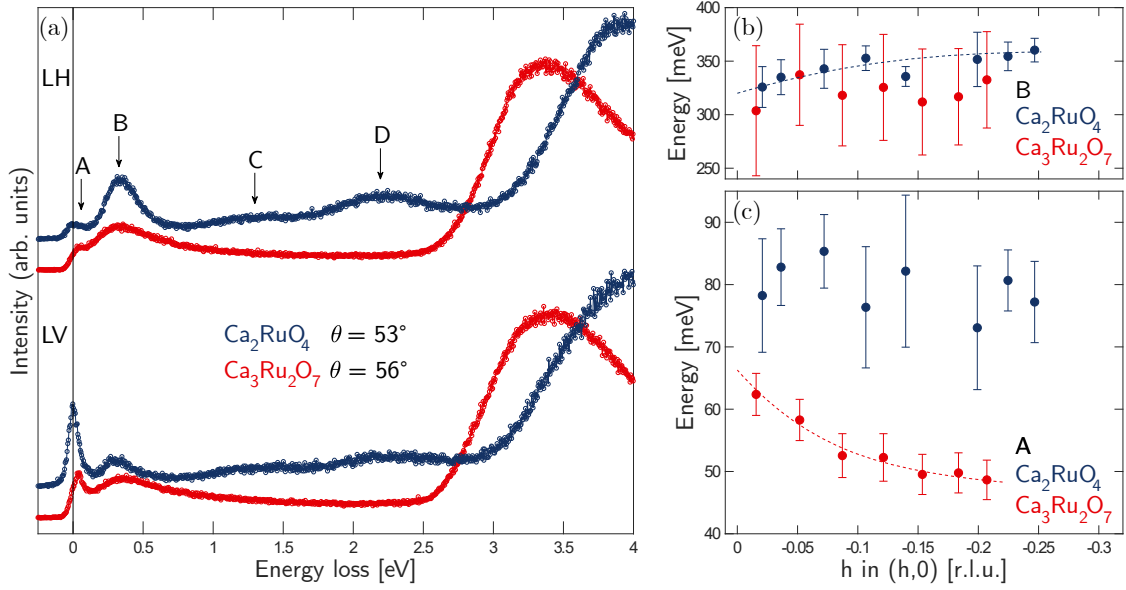


Figure 3.7.: (a) Comparison of LH and LV RIXS spectra of $\text{Ca}_3\text{Ru}_2\text{O}_7$ and Ca_2RuO_4 . Four low energy excitations A, B, C and D are found in Ca_2RuO_4 . (b), (c) energies of A and B excitations as a function of in-plane momentum h , extracted from $\text{Ca}_3\text{Ru}_2\text{O}_7$ LV (LH) spectra for A (B), and Ca_2RuO_4 LH spectrum. Errorbars on $\text{Ca}_3\text{Ru}_2\text{O}_7$ A excitation energies indicate standard deviation 3σ extracted from confidence intervals of the fitting parameter. For the B excitations, see appendix B. The A excitation shows a clear dispersion towards lower energies for increasing momentum in $\text{Ca}_3\text{Ru}_2\text{O}_7$. Ca_2RuO_4 data from Ref. [41].

of the four low energy excitations depends strongly on incident light polarization. In Ref. [41] it is discussed how the different excitations can be observed on the apical or planar site with LH or LV polarization. In comparison to theoretical modelling that is discussed in detail in the supplemental material of Ref. [41], they can be interpreted as a result of composite spin-orbital excitations. More precisely, excitations C and D are associated to single and double singlet-triplet excitations with energies defined by Hund's coupling ($2J_H$ and $4J_H$ respectively). The A and B excitations reflect the internal low energy scale configuration of the t_{2g} orbitals occupied by 4 electrons. Without spin-orbit-coupling λ , the threefold degenerate ground state sector α has a doubly occupied d_{xy} orbital (doublon) and the other two electrons forming a spin-triplet state. The lowest lying excitation sector β is sixfold degenerate with the doublon in the d_{xz} and d_{yz} orbitals. When finite spin-orbit-coupling is introduced, the degeneracies of the α and β states are lifted. Additionally, the orbital character of the doublon state is mixed and the β states hence correspond to spin orbital excitations. With this theoretical background, the A feature in the spectrum is assigned to magnetic excitations within the α sector

whereas the B feature is interpreted by β sector excitations.

In Fig. 3.7 (b), the momentum dependence along the Ru-O bond for A and B in Ca_2RuO_4 are shown again in dark blue. The peak maximum position reveals a very weak momentum dependence for the B feature, indicating a dispersive B sector with a minimum at the zone centre. For the A excitations, no dispersion could be observed within the experimental energy resolution.

Comparing $\text{Ca}_3\text{Ru}_2\text{O}_7$ and Ca_2RuO_4 spectra clear differences can be observed. First, the intense peak around 3.5 eV associated to dd excitation is shifted towards lower energies in $\text{Ca}_3\text{Ru}_2\text{O}_7$. Second, peaks C and D in Ca_2RuO_4 representing singlet-triplet excitations are completely absent in $\text{Ca}_3\text{Ru}_2\text{O}_7$. Lastly, peaks A and B are present in both compounds, but the peak shape, intensity and position of B clearly differs. In Ca_2RuO_4 , the peak has a distinct polarization dependence in intensity as well as in position. In contrast, the B peak in $\text{Ca}_3\text{Ru}_2\text{O}_7$ is much broader, less intense and shows almost no polarization dependence.

Looking at the momentum dependence of excitations A and B for both compounds in Fig. 3.7 (b), the differences of these two excitations become even more apparent. Due to the broadness of B, no dispersion can be observed for $\text{Ca}_3\text{Ru}_2\text{O}_7$. On the other hand, excitation A is consistently at significantly lower energies in $\text{Ca}_3\text{Ru}_2\text{O}_7$ compared to Ca_2RuO_4 and disperses strongly to lower energies for higher in-plane momentum h . This indicates that excitation A in $\text{Ca}_3\text{Ru}_2\text{O}_7$ represents a unique collective orbital excitation.

3.2.4. Discussion

The differences between Ca_2RuO_4 and $\text{Ca}_3\text{Ru}_2\text{O}_7$ in the RIXS spectra are not surprising considering the different magnetic and electronic ground states. As already mentioned for Ca_2RuO_4 , the c -axis compression lowers the energy of the d_{xy} orbital leaving it doubly occupied. The remaining two electrons in the d_{xz} and d_{yz} orbitals form a spin triplet with antiferromagnetic in-plane spin ordering. In $\text{Ca}_3\text{Ru}_2\text{O}_7$, the magnetic moments are ferromagnetically ordered in-plane. Having the same ferro-orbital order as in Ca_2RuO_4 with the doublon always on the same orbital, this would lead to a complete blocking of the electron itinerancy in the ab -plane. Hence, one would expect to have a different type of orbital ordering. Another indication for this scenario is the reduced c -axis compression in $\text{Ca}_3\text{Ru}_2\text{O}_7$ that may not lower the energy of the d_{xy} orbital enough to leave it doubly occupied on all ruthenium sites and drive the system Mott insulating on the other orbitals. Altogether, these theoretical considerations about an antiferro-orbital order in $\text{Ca}_3\text{Ru}_2\text{O}_7$ are supported by the experimental data presented in this work. Neither do the XAS data show a dependence on probing d_{xy} , d_{xz} or d_{yz} , nor are the excitations seen in RIXS

polarization dependent.

With such a type of ground state, $\text{Ca}_3\text{Ru}_2\text{O}_7$ will have spin and orbital excitations of different nature than Ca_2RuO_4 . A possible explanation for the low energy mode in $\text{Ca}_3\text{Ru}_2\text{O}_7$ would be orbital flip type excitations, where the doublon character on one ruthenium is changed and this excitation then propagates. This kind of excitations would not be sensitive to spin ordering and therefore the presence of these features in the RIXS spectra above the magnetic transition at 80 K is not surprising. However, other origins of the excitations can not be excluded and a complete explanation can not be given based on the data presented here. Additionally, a reason for the missing C and D excitations in $\text{Ca}_3\text{Ru}_2\text{O}_7$ is still lacking.

In summary, the RIXS data presented in this chapter reveal two low energy excitations A and B besides the dd excitation in $\text{Ca}_3\text{Ru}_2\text{O}_7$. Momentum dependent measurements of A show that this excitation is dispersing towards lower energy for increasing in-plane momentum and is therefore interpreted as a collective orbital excitation. Comparison to Ca_2RuO_4 reveals several significant differences in the spectrum: missing C and D excitations in $\text{Ca}_3\text{Ru}_2\text{O}_7$, shifted dd excitation peak and different shape, intensity and energy position for A and B. Most remarkably, the momentum dependence of the low energy excitations present in both compounds is clearly different.

4. Conclusion and Outlook

In materials that show an extremely diverse phase diagram like the ruthenates, the interplay of multiple competing energy scales leads to complex behaviour of lattice, spin and orbital degrees of freedom. In Ca_2RuO_4 , the insulating state can not be explained by a conventional Mott transition alone but rather by a combination of band and Mott physics. Hund's coupling also takes an important role since the intermediately filled $4d-t_{2g}$ manifold has a multi-orbital character. Additionally, the importance of spin-orbit coupling has been confirmed in the interpretation of low energy electronic excitations. Comparison of the double layer $\text{Ca}_3\text{Ru}_2\text{O}_7$ to this system therefore offers the opportunity to study the influence of structure on the relative strength of these different energy scales. Although there are many similarities between the two compounds, the low temperature electronic and magnetic properties of $\text{Ca}_3\text{Ru}_2\text{O}_7$ differ significantly from Ca_2RuO_4 and are not fully understood yet.

In this thesis, a comparative XAS and RIXS study of these two compounds is presented and differences in the low-lying electronic properties are identified. The oxygen K -edge absorption spectra of $\text{Ca}_3\text{Ru}_2\text{O}_7$ confirms the orbital selectivity of this method and shows distinct features depending on the oxygen site and hybridization with ruthenium t_{2g} and e_g orbitals. The comparison of different light polarizations and incident angles suggests that the inner apical oxygen O(a2) is very close in energy to the planar O(p). Furthermore, there was no temperature dependence observed in the absorption by crossing both structural and magnetic transitions. This is in contrast to the behaviour found in Ca_2RuO_4 . Additionally, the whole XAS spectrum of $\text{Ca}_3\text{Ru}_2\text{O}_7$ seems to be shifted towards lower energies compared to Ca_2RuO_4 . The RIXS spectra of $\text{Ca}_3\text{Ru}_2\text{O}_7$ show three features beside the elastic peak. A very intense and broad dd excitation and two low energy excitations A and B. All of them are almost independent of light polarization and do not change by crossing the magnetic and structural transition temperatures. Thus, these excitations are not likely to depend on spin ordering. Most remarkably, a detailed analysis of the momentum dependence reveals the dispersive character of the A feature. This collective orbital excitation is reported here for the first time and is unique for that compound as shown by a direct comparison to the single layer Ca_2RuO_4 . Additionally, two features in the RIXS spectrum of Ca_2RuO_4 are completely absent in $\text{Ca}_3\text{Ru}_2\text{O}_7$.

Altogether, the findings suggest that these differences are connected to the different electronic and magnetic ground states of these two materials. Whereas the in-plane momenta are antiferromagnetically ordered in Ca_2RuO_4 , they are ferromagnetically ordered in $\text{Ca}_3\text{Ru}_2\text{O}_7$. To preserve itinerancy in $\text{Ca}_3\text{Ru}_2\text{O}_7$, the orbital order of the t_{2g} manifold must be different from Ca_2RuO_4 , where ferro-orbital order is realised by a doubly occupied d_{xy} orbital on all ruthenium sites. However, the results presented here do not allow for an unambiguous conclusion about the relative occupancy of the t_{2g} orbitals.

Further investigations of the orbital occupancy with different techniques like polarization dependent ARPES or resonant scattering are necessary to resolve this question. Another possible next step are theoretical model calculations for both XAS and RIXS responses of the in-plane ferromagnetic ground state to support our findings and help for an interpretation of the low energy excitation spectrum. A more direct way of looking at the interesting physics happening in the Ru d orbitals is Ru L -edge RIXS that has been currently made accessible at PETRA-III (see section 3.1.1). Such a measurement has already been done on Ca_2RuO_4 by Gretarsson *et al.* [44]. In contrast to the findings presented here and in Ref. [41], they observe an additional excitation below 2 eV and hence obtain a different value for the Hund's coupling J_H . The excitation spectrum of Ca_2RuO_4 is therefore still controversial.

In general, RIXS is an extremely versatile technique that is routinely used to investigate many different types of excitations. Apart from the above mentioned orbital excitations, a lot of work has been done on magnons, phonons and even charge order. In appendix C, a Cu L -edge RIXS experiment on the cuprate superconductor $\text{La}_{1.68}\text{Eu}_{0.2}\text{Sr}_{0.12}\text{CuO}_4$ is presented, where charge order is measured in the quasi-elastic scattering contribution of the RIXS spectra.

Beyond the scope of standard RIXS experiments presented here, new advances are made in studying the time evolution of elementary excitations after a perturbation of the system. Such non-equilibrium measurements have been made possible by the development of extremely bright x-ray free-electron lasers (FEL). First time-resolved pump-probe RIXS measurements have already been made and a lot of effort is taken to enhance energy resolution in such experiments [50, 51]. Although FEL-based RIXS is a new and still developing technique, FEL facilities are regularly used as a source for other techniques like x-ray diffraction. Appendix D briefly summarizes the outcome of two XRD free-electron laser experiments performed at SACLA and SwissFEL with high magnetic field (47 Tesla) applied to $\text{La}_{1.88}\text{Sr}_{0.12}\text{CuO}_4$.

Appendix

A. Absorption Resonance Energy

To determine the energy of the apical and planar resonance, the low energy part of the XAS spectrum is fitted with the sum of three Gaussian line shape components to describe the two resonance peaks and the background from absorption resonances at higher energies:

$$I(E) = a_1 e^{-\left(\frac{E-b_1}{c_1}\right)^2} + a_2 e^{-\left(\frac{E-b_2}{c_2}\right)^2} + a_3 e^{-\left(\frac{E-b_3}{c_3}\right)^2}, \quad (\text{A.1})$$

where I is the measured intensity, E the incident photon energy and a_i , b_i and c_i are the amplitudes, positions and widths of the Gaussians. The absorption energies for apical and planar resonances are then extracted as the peak positions b_1/b_2 of the two fitted lower-energy Gaussians. Fig. A.1 shows an example of the fitting procedure. The value of the planar resonance in table 3.2 is extracted from LH grazing spectrum, as this experimental geometry probes the O(p) sites at low energies.

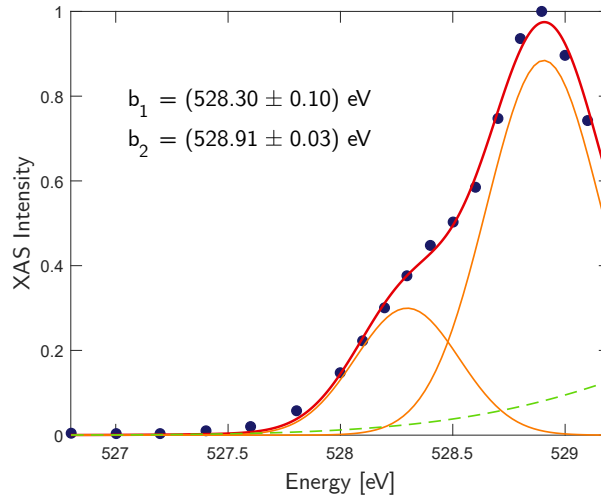


Figure A.1.: Low energy part of the LV normal incidence XAS spectrum illustrating the fitting procedure. The fit (red) is composed of two Gaussians (orange) and the tail of a third Gaussian as background (green dashed).

B. Analysis of B Excitation

In $\text{Ca}_3\text{Ru}_2\text{O}_7$, the B excitation around 350 meV is so broad, that its width is larger than the excitation energy. This indicates either that a quasiparticle picture is invalid or that the B feature is composed of more than one quasiparticle excitation which can not be resolved in this experiment. To assign an energy to this feature for comparison with the single layer data, the peak position is defined as the maximum evaluated as the zero of the derivative.

Because the data includes counting statistical noise, each spectrum is first smoothed by taking the Gaussian weighted average of data points in a variable binning window. To account for the dependence of the peak maximum on the window size, each spectrum is smoothed with window sizes between five and one hundred, see Fig. B.1 (a). The zero of the derivative is then extracted for all the differently smoothed data and plotted as function of window size. The actual peak position for the spectrum is the limit for window size zero defined as the y-intercept of a first order polynomial fit to the points, see Fig. B.1 (b). The first four data points are excluded in the fitting procedure. For these points, the window size is too small resulting in a non-representative peak maximum. The errorbars in Fig. 3.7 represent the peak width at 98% of the total height, evaluated from the smoothed data with window size 40.

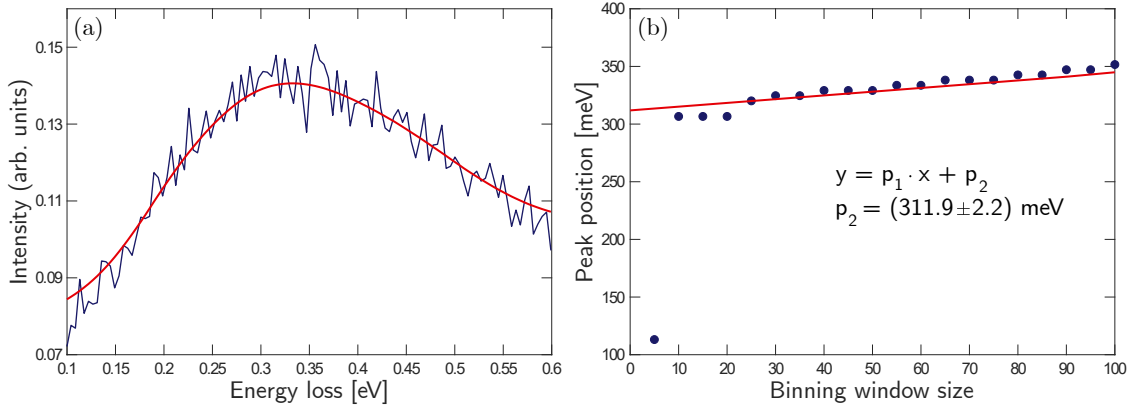


Figure B.1.: (a) Zoom on B excitation recorded with LH polarization and incident angle $\theta = 56^\circ$. Red line represents the data smoothed with Gaussian weighted average in a window of 40 data points. (b) Peak positions (defined as the zero of the derivative of smoothed data), as a function of the binning window size. Red line is a first order polynomial fit.

C. Charge-Density-Wave Order in LESCO

This section summarizes the outcome of RIXS experiments on $\text{La}_{1.68}\text{Eu}_{0.2}\text{Sr}_{0.12}\text{CuO}_4$ (LESCO), in which I participated during my master project. Apart from studying elementary excitations, RIXS is also a powerful technique to probe charge ordering phenomena by measuring the quasi-elastic scattering contribution of RIXS spectra. The advantage of RIXS over resonant elastic scattering (REXS) techniques is that the energy resolving power of RIXS allows to disentangle elastic from inelastic scattering processes. Here, a RIXS study on the temperature evolution of charge order in LESCO is summarized.

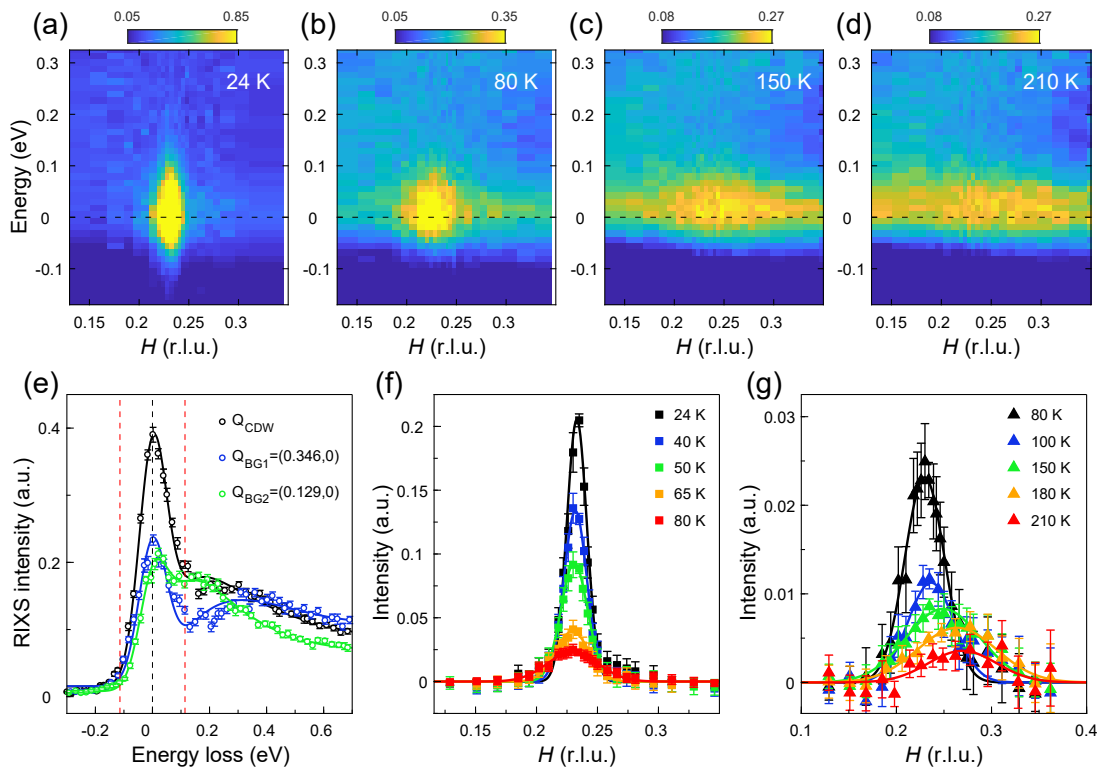


Figure C.1.: (a)-(d) Energy/momentum intensity maps of the RIXS spectra across the H direction for different temperatures. (e) Representative RIXS spectra showing data measured at the charge order peak and background positions. Vertical red dashed lines mark the energy window of the quasi-elastic intensity integration for (f) and (g). (f),(g) Background subtracted integrated quasi-elastic scans along the H direction for different temperatures. Taken from Ref. [52].

In LESCO, the low-temperature tetragonal (LTT) crystal structure phase sets in at 125 K and previous REXS experiments report charge-density-wave (CDW) ordering appearing only below 80 K. This discrepancy in temperature between the onset of

LTT structure and charge order suggests that they are not fundamentally correlated. However, the data obtained with RIXS presented here show that the CDW diffraction persists up to 210 K, well above the LTT phase. Fig. C.1 (a)-(d) show intensity maps of the Cu L_3 -edge RIXS spectra in energy-momentum space for different temperatures. At 24 K strong elastic scattering due to the CDW order is observed near relative momentum $H = 0.233$. On warming, the quasi-elastic peak intensity weakens but does not vanish completely. In Fig. C.1 (f),(g) the integrated quasi-elastic intensity in the RIXS maps are plotted as function of momentum H for temperatures up to 210 K. Most remarkably, the well defined peaks remain detectable far above the LTO-LTT structure transition. Upon warming up from base temperature towards the transition, the peak amplitude is reduced drastically and the peak width increases gradually. At higher temperatures, the main change is on the peak position which moves towards higher H . The temperature dependences of the CDW peak intensity, correlation length and wavevector Q_{CDW} are summarized in Fig. C.2. Both intensity and correlation length show a prominent change upon entering the LTT phase. In contrast, the wavevector of the CDW peak does not show any anomaly across the transition temperature but decreases gradually down to 80 K. In summary, the data presented here nicely illustrate the power of the RIXS technique even for quasi-elastic scattering studies.

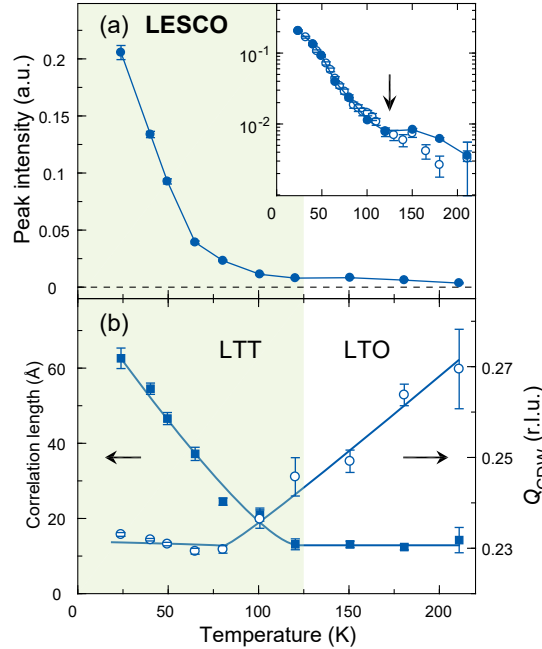


Figure C.2.: (a),(b) Temperature dependence of the CDW peak intensity, wavevector and correlation length in LESCO. Taken from Ref. [52].

D. Free-Electron Laser Experiments

In addition to the resonant x-ray scattering experiments on ruthenates and cuprates (appendix C), my master project included two hard x-ray diffraction (XRD) experiments conducted at free-electron laser (FEL) facilities: SACLA in Japan and SwissFEL in Switzerland. I have contributed in sample preparation, cryogenic instrumentation, experiment execution and data analysis. This section briefly describes the outcome of these two experiments on $\text{La}_{1.88}\text{Sr}_{0.12}\text{CuO}_4$.

The primary goal of the experiments was to search for novel field-induced charge order reflections. To this end, the femtosecond x-ray pulses from the FEL were synchronized with millisecond magnetic field pulses up to 47 T. Unfortunately, the signal-to-noise ratio was not sufficient to resolve the charge order peak. Instead, a large magnetostriction effect was observed on the lattice Bragg peak (2,0,12). This effect describes the change in lattice parameters upon applied magnetic field. In $\text{La}_{1.88}\text{Sr}_{0.12}\text{CuO}_4$, a relative change in the lattice parameter $\Delta c/c$ of 10^{-4} was measured as a shift in the 2θ position of the Bragg peak. Fig. D.1 (a) shows single shot 2D images of the detected Bragg peak without (left) and with (right) magnetic field pulse. As can be seen, the peak shifts to lower values of 2θ when a magnetic field is applied. In (b), the calculated relative change in the lattice parameter c is plotted as function of magnetic field.

Such pulsed magnetic field experiments have been made possible by the advent of FEL user facilities, since their bright and very short pulses provide enough intensity for measuring diffraction peaks within a single shot.

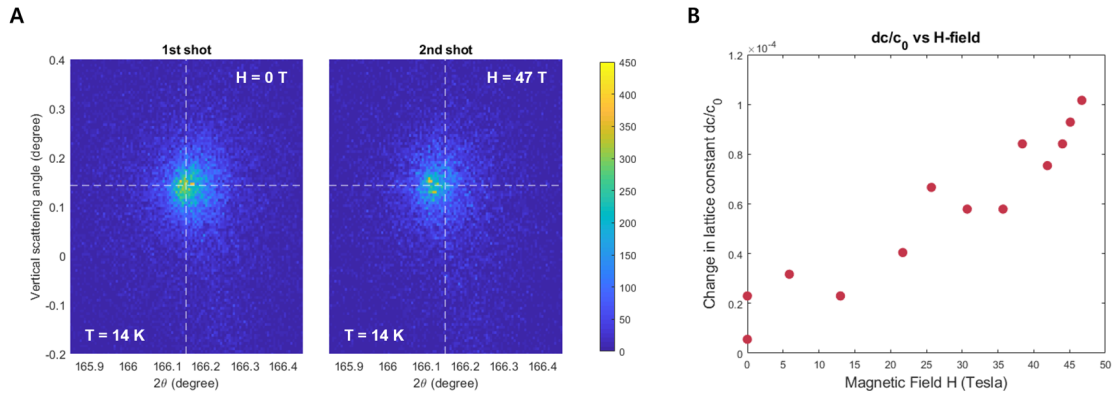


Figure D.1.: (a) Single shot image of the (2,0,12) Bragg peak as detected by the 2D detector under zero (left) and 47 T (right) external magnetic field. (b) Relative change of lattice parameter c as a function of magnetic field.

References

- [1] H. K. Onnes, “The resistance of pure mercury at helium temperatures,” *Commun. Phys. Lab. Univ. Leiden*, vol. 12, pp. 120+, 1911.
- [2] N. F. Mott, “The Basis of the Electron Theory of Metals, with Special Reference to the Transition Metals,” *Proc. Phys. Soc. A*, vol. 62, pp. 416–422, July 1949.
- [3] S. Jin, T. H. Tiefel, M. McCormack, R. A. Fastnacht, R. Ramesh, and L. H. Chen, “Thousandfold Change in Resistivity in Magnetoresistive La-Ca-Mn-O Films,” *Science*, vol. 264, pp. 413–415, Apr. 1994.
- [4] Y. Murakami, J. P. Hill, D. Gibbs, M. Blume, I. Koyama, M. Tanaka, H. Kawata, T. Arima, Y. Tokura, K. Hirota, and Y. Endoh, “Resonant X-Ray Scattering from Orbital Ordering in LaMnO₃,” *Phys. Rev. Lett.*, vol. 81, pp. 582–585, July 1998.
- [5] C. N. R. Rao, “Transition Metal Oxides,” *Annu. Rev. Phys. Chem.*, vol. 40, pp. 291–326, 1989.
- [6] Y. S. Lee, J. S. Lee, T. W. Noh, D. Y. Byun, K. S. Yoo, K. Yamaura, and E. Takayama-Muromachi, “Systematic trends in the electronic structure parameters of the 4d transition-metal oxides SrMO₃ ($M = \text{Zr, Mo, Ru, and Rh}$),” *Phys. Rev. B*, vol. 67, p. 113101, Mar. 2003.
- [7] G. Kotliar and D. Vollhardt, “Strongly Correlated Materials: Insights From Dynamical Mean-Field Theory,” *Physics Today*, vol. 57, pp. 53–59, Mar. 2004.
- [8] D. Sutter, *Strong Electron Correlations in the Ruthenates*. PhD thesis, Universität Zürich, Zürich, 2019.
- [9] E. Dagotto, “Complexity in Strongly Correlated Electronic Systems,” *Science*, vol. 309, pp. 257–262, July 2005.
- [10] Y. Tokura and N. Nagaosa, “Orbital Physics in Transition-Metal Oxides,” *Science*, vol. 288, pp. 462–468, Apr. 2000.

- [11] M. Braden, G. André, S. Nakatsuji, and Y. Maeno, “Crystal and magnetic structure of Ca_2RuO_4 : Magnetoelastic coupling and the metal-insulator transition,” *Phys. Rev. B*, vol. 58, pp. 847–861, July 1998.
- [12] O. Friedt, M. Braden, G. André, P. Adelman, S. Nakatsuji, and Y. Maeno, “Structural and magnetic aspects of the metal-insulator transition in $\text{Ca}_{2-x}\text{Sr}_x\text{RuO}_4$,” *Phys. Rev. B*, vol. 63, p. 174432, Apr. 2001.
- [13] A. Georges, L. d. Medici, and J. Mravlje, “Strong Correlations from Hund’s Coupling,” *Annu. Rev. Condens. Matter Phys.*, vol. 4, pp. 137–178, Apr. 2013.
- [14] N. Kikugawa, A. Winfried Rost, C. William Hicks, A. John Schofield, and A. Peter Mackenzie, “ $\text{Ca}_3\text{Ru}_2\text{O}_7$: Density Wave Formation and Quantum Oscillations in the Hall Resistivity,” *J. Phys. Soc. Jpn.*, vol. 79, p. 024704, Feb. 2010.
- [15] G. Cao, S. McCall, M. Shepard, J. E. Crow, and R. P. Guertin, “Thermal, magnetic, and transport properties of single-crystal $\text{Sr}_{1-x}\text{Ca}_x\text{RuO}_3$ ($0 \leq x \leq 1.0$),” *Phys. Rev. B*, vol. 56, no. 1, pp. 321–329, 1997.
- [16] Y. Yoshida, S.-I. Ikeda, H. Matsuhata, N. Shirakawa, C. H. Lee, and S. Katano, “Crystal and magnetic structure of $\text{Ca}_3\text{Ru}_2\text{O}_7$,” *Phys. Rev. B*, vol. 72, p. 054412, Aug. 2005.
- [17] S. McCall, G. Cao, and J. E. Crow, “Impact of magnetic fields on anisotropy in $\text{Ca}_3\text{Ru}_2\text{O}_7$,” *Phys. Rev. B*, vol. 67, p. 094427, Mar. 2003.
- [18] G. Cao, S. McCall, J. E. Crow, and R. P. Guertin, “Observation of a Metallic Antiferromagnetic Phase and Metal to Nonmetal Transition in $\text{Ca}_3\text{Ru}_2\text{O}_7$,” *Phys. Rev. Lett.*, vol. 78, pp. 1751–1754, Mar. 1997.
- [19] M. Zhu, J. Peng, T. Zou, K. Prokes, S. Mahanti, T. Hong, Z. Mao, G. Liu, and X. Ke, “Colossal Magnetoresistance in a Mott Insulator via Magnetic Field-Driven Insulator-Metal Transition,” *Phys. Rev. Lett.*, vol. 116, p. 216401, May 2016.
- [20] C. S. Nelson, H. Mo, B. Bohnenbuck, J. Stremper, N. Kikugawa, S. I. Ikeda, and Y. Yoshida, “Spin-charge-lattice coupling near the metal-insulator transition in $\text{Ca}_3\text{Ru}_2\text{O}_7$,” *Phys. Rev. B*, vol. 75, p. 212403, June 2007.
- [21] H. Xing, L. Wen, C. Shen, J. He, X. Cai, J. Peng, S. Wang, M. Tian, Z.-A. Xu, W. Ku, Z. Mao, and Y. Liu, “Existence of electron and hole pockets and partial gap opening in the correlated semimetal $\text{Ca}_3\text{Ru}_2\text{O}_7$,” *Phys. Rev. B*, vol. 97, p. 041113, Jan. 2018. arXiv: 1801.09048.

-
- [22] Y. Yoshida, I. Nagai, S.-I. Ikeda, N. Shirakawa, M. Kosaka, and N. Môri, “Quasi-two-dimensional metallic ground state of $\text{Ca}_3\text{Ru}_2\text{O}_7$,” *Phys. Rev. B*, vol. 69, p. 220411, June 2004.
- [23] G. Cao, L. Balicas, Y. Xin, J. E. Crow, and C. S. Nelson, “Quantum oscillations, colossal magnetoresistance, and the magnetoelastic interaction in bilayered $\text{Ca}_3\text{Ru}_2\text{O}_7$,” *Phys. Rev. B*, vol. 67, p. 184405, May 2003.
- [24] F. Baumberger, N. J. C. Ingle, N. Kikugawa, M. A. Hossain, W. Meevasana, R. S. Perry, K. M. Shen, D. H. Lu, A. Damascelli, A. Rost, A. P. Mackenzie, Z. Hussain, and Z.-X. Shen, “Nested Fermi Surface and Electronic Instability in $\text{Ca}_3\text{Ru}_2\text{O}_7$,” *Phys. Rev. Lett.*, vol. 96, p. 107601, Mar. 2006.
- [25] G. Cao, L. Balicas, Y. Xin, J. Crow, and C. Nelson, “Interplay between different degrees of freedom: unusual physical phenomena in $\text{Ca}_3\text{Ru}_2\text{O}_7$,” *Physica C: Superconductivity*, vol. 387, pp. 247–255, May 2003.
- [26] X. N. Lin, Z. X. Zhou, V. Durairaj, P. Schlottmann, and G. Cao, “Colossal Magnetoresistance by Avoiding a Ferromagnetic State in the Mott System $\text{Ca}_3\text{Ru}_2\text{O}_7$,” *Phys. Rev. Lett.*, vol. 95, p. 017203, June 2005.
- [27] W. Bao, Z. Q. Mao, Z. Qu, and J. W. Lynn, “Spin Valve Effect and Magnetoresistivity in Single Crystalline $\text{Ca}_3\text{Ru}_2\text{O}_7$,” *Phys. Rev. Lett.*, vol. 100, p. 247203, June 2008.
- [28] L. J. P. Ament, M. van Veenendaal, T. P. Devereaux, J. P. Hill, and J. van den Brink, “Resonant inelastic x-ray scattering studies of elementary excitations,” *Rev. Mod. Phys.*, vol. 83, pp. 705–767, June 2011.
- [29] N. B. Brookes, F. Yakhov-Harris, K. Kummer, A. Fondacaro, J. C. Cezar, D. Betto, E. Velez-Fort, A. Amorese, G. Ghiringhelli, L. Braicovich, R. Barrett, G. Berruyer, F. Cianciosi, L. Eybert, P. Marion, P. van der Linden, and L. Zhang, “The beamline ID32 at the ESRF for soft X-ray high energy resolution resonant inelastic X-ray scattering and polarisation dependent X-ray absorption spectroscopy,” *Nucl. Instrum. Methods Phys. Res. A*, vol. 903, pp. 175–192, Sept. 2018.
- [30] C. G. Fatuzzo, *Spectroscopic Studies of the Electronic Structure in Layered Cuprates and Ruthenates*. PhD thesis, Universität Zürich, Zürich, 2017.
- [31] V. N. Strocov, T. Schmitt, U. Flechsig, T. Schmidt, A. Imhof, Q. Chen, J. Raabe, R. Betemps, D. Zimoch, J. Krempasky, X. Wang, M. Grioni, A. Piazzalunga, and L. Patthey, “High-resolution soft X-ray beamline ADRESS at the Swiss Light

- Source for resonant inelastic X-ray scattering and angle-resolved photoelectron spectroscopies,” *J. Synchrotron Radiat.*, vol. 17, pp. 631–643, Sept. 2010.
- [32] F. Marschall, D. McNally, V. A. Guzenko, B. Rösner, M. Dantz, X. Lu, L. Nue, V. Strocov, T. Schmitt, and C. David, “Zone plates as imaging analyzers for resonant inelastic x-ray scattering,” *Opt. Express*, vol. 25, p. 15624, July 2017.
- [33] M. Minola, *Magnetic, Orbital and Charge Fluctuations in Layered Cuprates Studied by Resonant Soft X-Ray Scattering*. PhD thesis, Politecnico di Milano, 2013.
- [34] G. Ghiringhelli, A. Piazzalunga, C. Dallera, G. Trezzi, L. Braicovich, T. Schmitt, V. N. Strocov, R. Betemps, L. Patthey, X. Wang, and M. Grioni, “SAXES, a high resolution spectrometer for resonant x-ray emission in the 400 - 1600eV energy range,” *Rev. Sci. Instrum.*, vol. 77, p. 113108, Nov. 2006.
- [35] T. Schmitt, V. N. Strocov, K.-J. Zhou, J. Schlappa, C. Monney, U. Flechsig, and L. Patthey, “High-resolution resonant inelastic X-ray scattering with soft X-rays at the ADDRESS beamline of the Swiss light source: Instrumental developments and scientific highlights,” *J Electron Spectros Relat Phenomena*, vol. 188, pp. 38–46, June 2013.
- [36] M. Soman, D. Hall, J. Tutt, N. Murray, A. Holland, T. Schmitt, J. Raabe, and B. Schmitt, “Developing a CCD camera with high spatial resolution for RIXS in the soft X-ray range,” *Nucl. Instrum. Methods Phys. Res. A*, vol. 731, pp. 47–52, Dec. 2013.
- [37] C. Monney, T. Schmitt, C. E. Matt, J. Mesot, V. N. Strocov, O. J. Lipscombe, S. M. Hayden, and J. Chang, “Resonant inelastic x-ray scattering study of the spin and charge excitations in the overdoped superconductor $\text{La}_{1.77}\text{Sr}_{0.23}\text{CuO}_4$,” *Phys. Rev. B*, vol. 93, p. 075103, Feb. 2016.
- [38] J. J. Sakurai, *Advanced Quantum Mechanics*. Addison-Wesley, Reading, MA, 1967.
- [39] S. Jöhr, *Removing Domain Boundaries in La_2CuO_4 , $\text{Ca}_3\text{Ru}_2\text{O}_7$ and $\text{YBa}_2\text{Cu}_3\text{O}_{7-x}$ using a Thermo-Mechanical Detwinning Device*. Bachelor Thesis, Universität Zürich, Zürich, Feb. 2019.
- [40] C. G. Fatuzzo, M. Dantz, S. Fatale, P. Olalde-Velasco, N. E. Shaik, B. Dalla Piazza, S. Toth, J. Pelliciari, R. Fittipaldi, A. Vecchione, N. Kikugawa, J. S. Brooks, H. M. Rønnow, M. Grioni, C. Rüegg, T. Schmitt, and J. Chang, “Spin-orbit-induced orbital excitations in Sr_2RuO_4 and Ca_2RuO_4 : A resonant inelastic x-ray scattering study,” *Phys. Rev. B*, vol. 91, p. 155104, Apr. 2015.

- [41] L. Das, F. Forte, R. Fittipaldi, C. Fatuzzo, V. Granata, O. Ivashko, M. Horio, F. Schindler, M. Dantz, Y. Tseng, D. McNally, H. Rønnow, W. Wan, N. Christensen, J. Pelliciani, P. Olalde-Velasco, N. Kikugawa, T. Neupert, A. Vecchione, T. Schmitt, M. Cuoco, and J. Chang, “Spin-Orbital Excitations in Ca_2RuO_4 Revealed by Resonant Inelastic X-Ray Scattering,” *Phys. Rev. X*, vol. 8, p. 011048, Mar. 2018.
- [42] I. Zegkinoglou, J. Strempfer, C. S. Nelson, J. P. Hill, J. Chakhalian, C. Bernhard, J. C. Lang, G. Srajer, H. Fukazawa, S. Nakatsuji, Y. Maeno, and B. Keimer, “Orbital Ordering Transition in Ca_2RuO_4 Observed with Resonant X-Ray Diffraction,” *Phys. Rev. Lett.*, vol. 95, p. 136401, Sept. 2005.
- [43] H. Suzuki, H. Gretarsson, H. Ishikawa, K. Ueda, Z. Yang, H. Liu, H. Kim, D. Kukusta, A. Yaresko, M. Minola, J. A. Sears, S. Francoual, H.-C. Wille, J. Nuss, H. Takagi, B. J. Kim, G. Khaliullin, H. Yavas, and B. Keimer, “Spin waves and spin-state transitions in a ruthenate high-temperature antiferromagnet,” *Nat. Mater.*, vol. 18, pp. 563–567, June 2019. arXiv: 1904.01930.
- [44] H. Gretarsson, H. Suzuki, H. Kim, K. Ueda, M. Krautloher, B. J. Kim, H. Yavas, G. Khaliullin, and B. Keimer, “Observation of spin-orbit excitations and Hund’s multiplets in Ca_2RuO_4 ,” *arXiv:1906.01221 [cond-mat]*, June 2019. arXiv: 1906.01221.
- [45] M. M. Sala, M. Rossi, S. Boseggia, J. Akimitsu, N. B. Brookes, M. Isobe, M. Minola, H. Okabe, H. M. Rønnow, L. Simonelli, D. F. McMorrow, and G. Monaco, “Orbital occupancies and the putative $j_{\text{eff}} = 1/2$ ground state in Ba_2IrO_4 : A combined oxygen K -edge XAS and RIXS study,” *Phys. Rev. B*, vol. 89, p. 121101, Mar. 2014.
- [46] T. Mizokawa, L. H. Tjeng, G. A. Sawatzky, G. Ghiringhelli, O. Tjernberg, N. B. Brookes, H. Fukazawa, S. Nakatsuji, and Y. Maeno, “Spin-Orbit Coupling in the Mott Insulator Ca_2RuO_4 ,” *Phys. Rev. Lett.*, vol. 87, p. 077202, July 2001.
- [47] M. Malvestuto, E. Carleschi, R. Fittipaldi, E. Gorelov, E. Pavarini, M. Cuoco, Y. Maeno, F. Parmigiani, and A. Vecchione, “Electronic structure trends in the $\text{Sr}_{n+1}\text{Ru}_n\text{O}_{3n+1}$ family ($n = 1,2,3$),” *Phys. Rev. B*, vol. 83, p. 165121, Apr. 2011.
- [48] C. T. Chen, L. H. Tjeng, J. Kwo, H. L. Kao, P. Rudolf, F. Sette, and R. M. Fleming, “Out-of-plane orbital characters of intrinsic and doped holes in $\text{La}_{2-x}\text{Sr}_x\text{CuO}_4$,” *Phys. Rev. Lett.*, vol. 68, pp. 2543–2546, Apr. 1992.
- [49] T. Mizokawa, L. H. Tjeng, H.-J. Lin, C. T. Chen, S. Schuppler, S. Nakatsuji, H. Fukazawa, and Y. Maeno, “Orbital state and metal-insulator transition in

- $\text{Ca}_{2-x}\text{Sr}_x\text{RuO}_4$ ($x = 0.0$ and 0.09) studied by x-ray absorption spectroscopy,” *Phys. Rev. B*, vol. 69, p. 132410, Apr. 2004.
- [50] M. P. M. Dean, Y. Cao, X. Liu, S. Wall, D. Zhu, R. Mankowsky, V. Thampy, X. M. Chen, J. G. Vale, D. Casa, J. Kim, A. H. Said, P. Juhas, R. Alonso-Mori, J. M. Glowina, A. Robert, J. Robinson, M. Sikorski, S. Song, M. Kozina, H. Lemke, L. Patthey, S. Owada, T. Katayama, M. Yabashi, Y. Tanaka, T. Togashi, J. Liu, C. Rayan Serrao, B. J. Kim, L. Huber, C.-L. Chang, D. F. McMorrow, M. Först, and J. P. Hill, “Ultrafast energy- and momentum-resolved dynamics of magnetic correlations in the photo-doped Mott insulator Sr_2IrO_4 ,” *Nature Mater*, vol. 15, pp. 601–605, June 2016.
- [51] M. Dell’Angela, F. Hieke, M. Malvestuto, L. Sturari, S. Bajt, I. V. Kozhevnikov, J. Ratanapreechachai, A. Caretta, B. Casarin, F. Glerean, A. M. Kalashnikova, R. V. Pisarev, Y.-D. Chuang, G. Manzoni, F. Cilento, R. Mincigrucci, A. Simoncig, E. Principi, C. Masciovecchio, L. Raimondi, N. Mahne, C. Svetina, M. Zangrando, R. Passuello, G. Gaio, M. Prica, M. Scarcia, G. Kourousias, R. Borghes, L. Giannessi, W. Wurth, and F. Parmigiani, “Extreme ultraviolet resonant inelastic X-ray scattering (RIXS) at a seeded free-electron laser,” *Sci Rep*, vol. 6, p. 38796, Dec. 2016.
- [52] Q. Wang, M. Horio, K. von Arx, D. Mukkattukavil, Y. Sassa, S. Pyon, T. Takayama, H. Takagi, Y. Tseng, W. Zhang, T. Schmitt, and J. Chang, “High Temperature Charge-Density-Wave Order in $(\text{La},\text{Eu})_{1.88}\text{Sr}_{0.12}\text{CuO}_4$,” *In preparation*, 2019.

Acknowledgements

During the last year I was happy to work together with a lot of very supportive people in the different projects I joined. First and foremost, a special thank goes to my supervisor Prof. Johan Chang, who gave me the opportunity to contribute and be part of his group. I am grateful for all the countless discussions, the valuable and honest advice, for challenging and supporting me whenever he could. I benefited enormously from his encouraging guidance and he helped me to expand my knowledge concerning all aspects of science.

During the different experiments I received a lot of help and support from collaborators and beamline scientists. In particular, I would like to thank Thorsten Schmitt who helped me with his expertise in RIXS and took time to answer all my questions. For fruitful discussions and inputs on the theoretical side I would like to thank Mario Cuoco and Fiona Forte.

Many thanks go to Masafumi for introducing me to RIXS and guiding me through all the steps from the experiment over data analysis up to writing my thesis. His kind support and valuable feedback have been a great help and I especially thank him for his patience in answering all my numerous questions. For welcoming me in their office, I thank him together with Kevin and Qisi. They always provided good advice and help on all kind of things from travel tips to Matlab tricks. I would also like to thank all the other group members, especially Jaewon for challenging times at FEL experiments and Lakshmi for all the laughter and craziness we shared. For last-minute proofreading, big thanks go to Kevin, Qisi and Jaewon.

Finally, I want to thank my family and friends, without them I would have never made it here. Special thanks go to my fellow students who went through all the intense exam periods with me but also for the good time outside lecture halls. I am grateful to Sarah and Mättu for balancing out intense times during my studies. Endless support and encouragement always come from my mother Kornelia and my brother Lukas, for which I am so grateful!

Curriculum vitae

Karin von Arx

Tellistrasse 2

4622 Egerkingen

kvonar@physik.uzh.ch

Education

- 2017-2019 **Master of Science in Physics**
UZH, Laboratory for Quantum Matter REsearch, Group J. Chang
- 2017 **English Language School**
Cambridge Advanced Certificate, ELC Eastbourne, UK
- 2013-2016 **Bachelor of Science in Physics**
UZH, Surface Physics, Group J. Osterwalder
- 2008-2012 **Matura (Swiss university entrance qualification)**
Kantonsschule Olten, Switzerland

Conferences and Schools

- 2019 **MaNEP Winter School**
"Symmetry and topology: New twists in condensed matter", Switzerland
- 2019 **NGSCES 2019 International Conference**
Contributed talk "Comparative XAS and RIXS study of Ca_2RuO_4 and $\text{Ca}_3\text{Ru}_2\text{O}_7$ ", Italy September 2-6, 2019

Teaching

- 2014-2019 **Teaching Assistant**
UZH, assistant to exercise classes and lab for physics bachelor courses

Publications

- J. Choi, O. Ivashko, N. Dennler, D. Aoki, **K. von Arx**, S. Gerber, O. Gutowski, M. H. Fischer, J. Strempfer, M. v. Zimmermann, and J. Chang;
Pressure-induced rotational symmetry breaking in URu_2Si_2
Phys. Rev. **B** 98, 241113 (2018)
- **K. von Arx**, M. Horio, Q. Wang, L. Das, F. Forte, R. Fittipaldi, C. G. Fatuzzo, V. Granata, O. Ivashko, F. Schindler, M. Dantz, Yi Tseng, D. McNally, H. M. Rønnow, W. Wan, N. B. Christensen, J. Pelliciari, P. Olalde-Velasco, N. Kikugawa, T. Neupert, A. Vecchione, T. Schmitt, M. Cuoco, J. Chang;
Comparative Resonant Inelastic X-ray Scattering study of Ca_2RuO_4 and $Ca_3Ru_2O_7$
In preparation
- Q. Wang, M. Horio, **K. von Arx**, D. Mukkattukavil, Y. Sassa, S. Pyon, T. Takayama, H. Takagi, Y. Tseng, W. Zhang, T. Schmitt, J. Chang;
High Temperature Charge-Density-Wave Order in $(La, Eu)_{1.88}Sr_{0.12}CuO_4$
In preparation
- P. Kliuiev, G. Zamborlini, M. Jugovac, Y. Gurdal, **K. von Arx**, K. Waltar, S. Schnidrig, R. Alberto, M. Iannuzzi, V. Feyer, M. Hengsberger, J. Osterwalder, L. Castiglioni;
Valence electronic structure of a hydrogen evolution catalyst: orbital tomography of Co-pyrphyrin
In preparation